Continuum Mech. Thermodyn. (2026) 38:75
https://doi.org/10.1007/s00161-026-01498-w

ORIGINAL ARTICLE

Paweł Hołobut · Michał Majewski · Katarzyna Kowalczyk-Gajewska

Quantifying the effects of particle spatial distribution in random thermoelastic composites – numerical and mean-field analyses

Received: 15 April 2026 / Accepted: 1 June 2026

Abstract The effect of spatial distribution of randomly-placed particles in a representative composite volume on the thermoelastic effective properties and local stress and strain distribution is analyzed. Quantitative assessment is performed using both the full-field finite element analyses and the mean-field interaction model, known also as a "cluster" model. The latter model is developed in the multi-family setting enabling one to study the mean stress and strain separately for each inclusion in the representative unit cell. The particles are assumed to be spherical and of equal size, while considered examples differ by the volume fraction of inclusions and the particle spatial layout, and in particular the mean nearest-neighbour distances.

Keywords Composite materials · Thermoelasticity · Micro-mechanics · Packing and spatial distribution effects

1 Introduction

Nowadays, novel advanced materials are created not only by modification of material composition, e.g. by new alloying additions in metal alloys, but also by tailoring the material microstructure or nanostructure by optimized processing routes [1]. Micromechanics provides a powerful tool for the effective design of such processes as it enables one to estimate the macroscopic effective properties of heterogeneous materials knowing the local constitutive laws for the phases at the micro-level and morphological features of components within the representative volume. The key role in the micromechanical modelling is played by a micro-macro transition scheme (averaging rule) that makes it possible to estimate the sensitivity of the overall response to the changes in microstructure and local properties [2].

With respect to their microstructure, heterogeneous materials can be subdivided into those with periodic substructure and those with random but statistically homogeneous one. In the first case, a unit cell for the microstructure can be defined which by its replication in three directions fills the material volume. Materials with this type of microstructure are mainly synthetic ones like e.g. meta-materials produced by additive manufacturing. In the second case, the substructure can be characterized by a set of statistical distribution functions of some microstructrural parameters, e.g. size and shape distributions or various n-point correlation functions [3] such as the mean minimum distance between the particles. Development and validation of a

P. Hołobut · K. Kowalczyk-Gajewska (✉)
Institute of Fundamental Technological Research, Polish Academy of Sciences, Pawinskiego 5B, Warsaw 02-106, Poland
E-mail: kkowalcz@ippt.pan.pl

P. Hołobut
E-mail: pholob@ippt.pan.pl

M. Majewski
Polish-Japanese Academy of Information Technology, Koszykowa 86, Warsaw 02-008, Poland
E-mail: mmajew@pjwstk.edu.pl

Published online: 23 July 2026

mean-field model of particulate composites with random particle distribution will be the subject of the present paper.

While the use of numerical homogenization, in which the actual microstructure of a material can be directly subjected to mechanical analysis [4–6], seems to be the obvious choice to study the impact of microstructural features on the overall composite response, such an approach is still relatively time-consuming. The use of analytical models allows testing many scenarios and better understanding of the microstructure-property relationship. The majority of existing analytical mean-field models are based on the Eshelby solution. The solution applies to a *single ellipsoidal inclusion* in an infinite linearly elastic medium, subjected to a homogeneous external load at infinity. The Mori-Tanaka method based on this solution is the most widely used for composite materials. The model assumes that a single inclusion, being the representative of all the inhomogeneities in the representative volume, interacts only with the surrounding matrix while direct interactions between inclusions are neglected, which limits the applicability of the model to relatively small volume fractions. The other possibilities are the self-consistent and generalized self-consistent models, or differential and incremental schemes, which improve the predictions for higher volume contents or increased contrast between the phase properties, mainly by modifying the infinite matrix properties when applying the Eshelby result, cf. [2,7].

Unfortunately, the above-mentioned classical models fail to describe properly the effects of spatial distribution of inhomogeneities within the sample, which may be an important source of a material's anisotropy, even if it is composed of isotropic phases, as well as they neglect the variability of mean strains and stresses within the individual inclusions. The issue of microstructure-induced anisotropy was studied in more detail in the previous paper by the authors [8]. Let us only mention that [9] distinguished two classes of approaches to dealing with the anisotropic effect of regular particle distribution: i. homogenization models based on the one-particle approximation, e.g.: [10–13]; and ii. analytical or semi-analytical solutions for periodic arrangements of inhomogeneities, e.g.: [14–16]. We note that in [14] the method was developed for spheroidal inhomogeneities which were arbitrarily placed in the unit cell. The packing effect (but not the spatial distribution effect) can also be accounted for by the so-called morphologically representative pattern (MRP) approach developed in [17,18] and verified through comparison with numerical homogenization in [19] and [20] for elastic and elastic-plastic composites, respectively. An extensive review of the mentioned approaches can be found in [8,21] or [9].

In [8], when considering elastic-plastic composites with regular particle distribution, we selected and developed a different approach, originally proposed in [22] – **the cluster interaction model**, which includes the effect of morphological and spatial distribution of particles through the approximate solution of the Lippman-Schwinger-Dyson equation and the analytical result for *two interacting ellipsoidal inclusions* in the infinite medium by [23]. The model was later extended to coated inclusions [24] and thermoelasticity [25]. The approach was also adopted to derive the thermal conductivity of a composite with coated inclusions in [26]. Recently, an extension of the approach to viscoplastic and elastic-viscoplastic composites was formulated by combining the scheme with the tangent additive law [21]. An attempt at experimental validation of the effect was presented in [27] where samples with regular pores were produced using a 3D printing technique and tested in the regime of small strain to assess the anisotropy of elastic stiffness. In all contributions above, the validation and computational examples concern the single family variant of the method.

Following the problem review above, the goal of this research is two-fold: (i) development of efficient computational procedures for the multi-family variant of the cluster model and its broad verification, and (ii) analysis of the effect of spatial packing on the overall thermoelastic properties and local response of particulate composites. To our best knowledge, a mean-field model for thermoelastic metal matrix composites with comparable predictive capabilities, as concerns the response of individual inclusions in the representative volume, is not available in the existing literature. The proposed approach is foreseen to facilitate the study of damage development in composite materials, enabling assessment of different thresholds of damage initiation depending on the spatial distribution of particles and in particular the level of particle clustering [28,29]. Such variation was observed employing numerical homogenization techniques [5,30,31]. These studies demonstrated that while clustering has minimal influence on the overall elastic properties, it leads to the increased spread of mean fields between particles. Furthermore, they showed that the damage growth rate of a composite with a higher degree of clustering is significantly faster than for composites with a lower degree of clustering. Similarly, in [32] the outcomes of numerical simulations combining multipole expansion of local fields with the multi-particle unit cell method demonstrated that statistics of the peak stresses in a porous material with a random arrangement of pores is directly related to the statistics of nearest neighbours. The study compared random microstructures containing pore clusters of circular and elliptic shape with the ones containing uniformly distributed pores. It is noted that [33] also incorporated direct interactions between inclusions exploiting

the solution of [23] in the study of elastic-plastic composites, however, without introducing the concept of the cluster. The authors considered a random inclusion arrangement in the representative volume without its periodic extension to fill the whole space. In the same manner, a finite set of arbitrarily arranged elastically interacting spherical particles with the Gurtin–Murdoch type interfaces was studied in [34]. For that purpose the authors exploited the analytical solution in terms of a series expansion for a single-inhomogeneity under arbitrary far-field loading and the superposition principle.

The paper consists of five sections. After the present introductory part, the formulation of the cluster interaction scheme in the context of the thermoelastic constitutive law is provided in Section 2. The attention is focused on the multi-family variant of the method relevant for random particulate composites. Section 3 discusses details of the numerical finite element calculations performed to validate the approach. In Section 4, the variability of effective thermoelastic properties induced by specific arrangements of particles and the validity of results obtained by the analytical model are analyzed. In particular, the effect of the mean nearest-neighbour distance, as one of the parameters commonly used to describe the particle packing [35], is quantified. Two aluminum-alloy composite materials developed in [36], as well as a porous material and a material with very hard inclusions, are studied. Moreover, the variability of local mechanical fields in the particles is analyzed. The paper closes with conclusions. Additionally, two appendices provide the details of the calculation algorithm for the multi-family variant of the cluster model and discuss the necessary cluster size to achieve convergent results.

The following notation is used for vector and tensor operations: the full contraction of the second-order tensor $\mathbf{a}$ with the fourth-order tensor $\mathbb{A}$, resulting in another second-order tensor $\mathbf{b}$, is denoted by the ' $\cdot$ ' symbol: $\mathbf{b} = \mathbb{A} \cdot \mathbf{a}$ or $\mathbf{b} = \mathbf{a} \cdot \mathbb{A}$ meaning $b_{ij} = A_{ijkl} a_{kl}$ or $b_{ij} = a_{kl} A_{klij}$ in the components of the quantities in any orthonormal basis; the partial contraction of two fourth-order tensors $\mathbb{A}$ and $\mathbb{B}$ resulting in another fourth-order tensor $\mathbb{C}$ is denoted as: $\mathbb{C} = \mathbb{A}\mathbb{B}$ meaning $C_{ijkl} = A_{ijmn} B_{mnkl}$. Summation convention over repeated indices is used when not stated otherwise.

2 Mean-field interaction model for thermoelastic composites

In the interaction model, proposed originally by [22] for elastic composites, the composite microstructure is represented by an elementary cubic volume (a representative unit cell RUC) containing a finite number N of particles. When periodically reproduced, the RUC is filling the whole space. In this paper we assume a random spatial layout of spherical particles of equal sizes in the elementary volume, which is periodic at its boundaries (strictly speaking, a quasi-random arrangement of particles is considered). To each inclusion of the RUC we assign a set of inclusions which are its periodic images in the filled space. All inclusions in the set are supposed to be subjected to the same thermomechanical fields. This set of geometrically equivalent particles is called *a family*. Contrary to regular arrangements studied in [8], the inclusions within the RUC are not symmetrically equivalent and may exhibit different mean strains and stresses, so the number of families in this case is equal to the number N of inclusions in the RUC. As a consequence, a multi-family variant of the cluster model is required in the present study. We concentrate our attention on the effect of particle clustering on the effective properties as well as stress and strain heterogeneity among different particles within the cell stemming from their location with respect to the neighboring particles.

The mean-field interaction model (also known as a cluster model) was extended to the thermoelastic composite materials in [25]. The core idea of the model is to account for interactions between each pair of inclusions within the analyzed space, in addition to interactions between the inclusions and the matrix, by using the fundamental solution by Green's function technique (see [23]). Since, according to this solution, mutual interactions experienced by the selected inclusion in the RUC decay when the distance to the other inclusion increases, the analysis is restricted only to those inclusions which are contained in some material sub-volume of spherical shape. This spherical sub-domain, denoted in [22] as a 'cluster', is centered in the selected inclusion for which the influence of such interactions is assessed. The radius of the interaction sub-domain is established by some preliminary studies. In the considered examples, the radius 10 times larger than the RUC size was found to be sufficient (see Appendix B). The notion of a 'cluster' used here should not be confused with a group of clustered particles forming the densely-packed subregion of a RUC considered in [5] or [32] - the interaction cluster model accounts for any spatial distribution of particles.

The basic relations of the model developed in [25] are now recalled. The proposed efficient computational procedure is provided in the Appendix A. The local constitutive relation between the stress $\boldsymbol{\sigma}$ and strain $\boldsymbol{\varepsilon}$ in

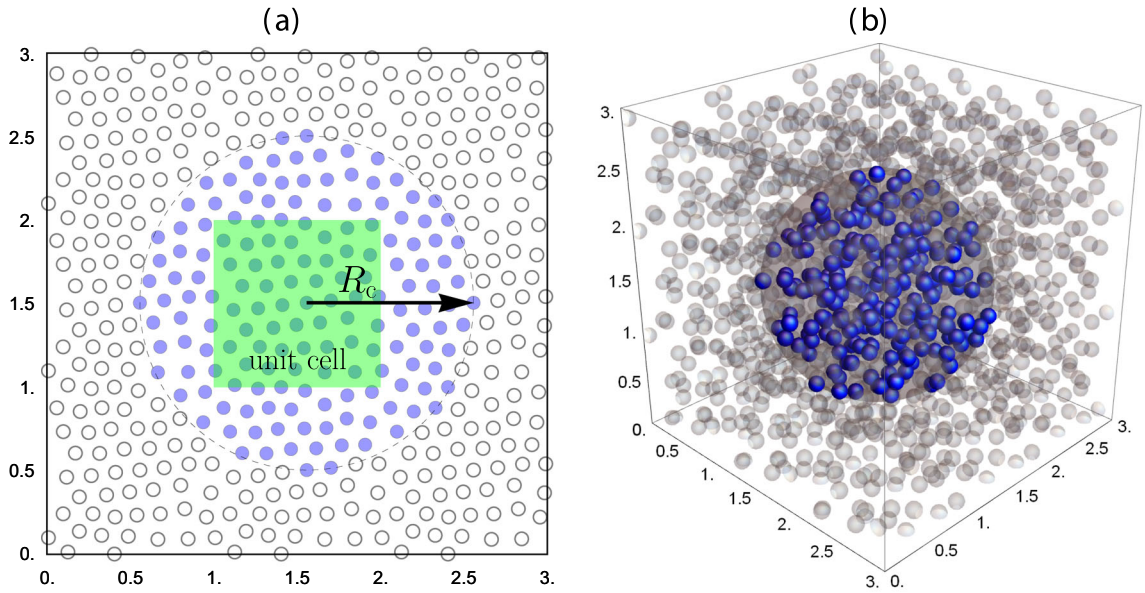

Fig. 1 **(a)** 2D cluster composed of the inclusions (in blue) whose centers are on or inside the circle of radius R_c.**(b)** 3D cluster.

each phase r is formulated as follows

$$\boldsymbol{\sigma} = \mathbb{C}_r \cdot \boldsymbol{\varepsilon} - \boldsymbol{\beta}_r \theta \,, \tag{1}$$

where $\mathbb{C}_r$ is the fourth-order stiffness tensor for phase r, and $\boldsymbol{\beta}_r\theta$ is the thermal stress at temperature change θ uniform in the composite ($\boldsymbol{\beta}_r = \mathbb{C}_r \cdot \boldsymbol{\alpha}_r$, and $\boldsymbol{\alpha}_r$ is the linear thermal expansion tensor). A two-phase composite is considered, so all inclusions in the RUC have the same material properties uniform per phase: $\mathbb{C}_\mathrm{i}$, $\boldsymbol{\beta}_\mathrm{i}$. The respective matrix properties are denoted by $\mathbb{C}_\mathrm{m}$ and $\boldsymbol{\beta}_\mathrm{m}$. Similar relations are also valid for the respective mean values $\boldsymbol{\sigma}_I = \langle\boldsymbol{\sigma}\rangle_I$ and $\boldsymbol{\varepsilon}_I = \langle\boldsymbol{\varepsilon}\rangle_I$ over volume V_I occupied by family I ($I = 1, \ldots, N$). $< \,.\, >_I = 1/V_I \int_{V_I}(.)\,\mathrm{dV}$ denotes the operation of volume averaging over the inclusions belonging to the family I, as well as for the matrix, namely:

$$\boldsymbol{\sigma}_I = \mathbb{C}_\mathrm{i} \cdot \boldsymbol{\varepsilon}_I - \boldsymbol{\beta}_\mathrm{i}\theta \,, \quad \boldsymbol{\sigma}_\mathrm{m} = \mathbb{C}_\mathrm{m} \cdot \boldsymbol{\varepsilon}_\mathrm{m} - \boldsymbol{\beta}_\mathrm{m}\theta \,. \tag{2}$$

As in any mean-field model, the effective stiffness tensor $\bar{\mathbb{C}}$ and effective thermal stress $\bar{\boldsymbol{\beta}}\theta$ can be found for the composite representative volume V, such that

$$\bar{\boldsymbol{\sigma}} = \sum_{I=1}^{N} f_I \boldsymbol{\sigma}_I + (1 - f_\mathrm{i})\boldsymbol{\sigma}_\mathrm{m} = \bar{\mathbb{C}} \cdot \bar{\boldsymbol{\varepsilon}} - \bar{\boldsymbol{\beta}}\theta \,, \quad \bar{\boldsymbol{\varepsilon}} = \sum_{I=1}^{N} f_I \boldsymbol{\varepsilon}_I + (1 - f_\mathrm{i})\boldsymbol{\varepsilon}_\mathrm{m} \,, \tag{3}$$

where f_i is the volume fraction of all inclusions in the RUC and $\sum_I f_I = f_\mathrm{i}$. As the local constitutive law is affine with $\mathbb{C}_r$ and $\boldsymbol{\beta}_r$ uniform per phase, the effective properties are specified using the relevant mechanical strain localization tensors $\mathbb{A}_I$ and $\mathbb{A}_\mathrm{m}$ of the fourth order:

$$\bar{\mathbb{C}} = \mathbb{C}_\mathrm{i} \left(\sum_{I=1}^{N} f_I \mathbb{A}_I \right) + (1 - f_\mathrm{i})\mathbb{C}_\mathrm{m}\mathbb{A}_m \,, \tag{4}$$

$$\bar{\boldsymbol{\beta}} = \boldsymbol{\beta}_\mathrm{i} \cdot \left(\sum_{I=1}^{N} f_I \mathbb{A}_I \right) + (1 - f_\mathrm{i})\boldsymbol{\beta}_\mathrm{m} \cdot \mathbb{A}_\mathrm{m} \,. \tag{5}$$

Based on (4) and (5), the mechanical strain localization tensor for the whole inclusion phase can be specified as:

$$\mathbb{A}_\mathrm{i} = \frac{1}{f_\mathrm{i}} \sum_{I=1}^{N} f_I \mathbb{A}_I \,. \tag{6}$$

The mean strain in each inclusion in the RUC, as a mean strain for the given family, and the mean-strain in the matrix phase can be specified separately by the strain localization relations of a standard form

$$\boldsymbol{\varepsilon}_I = \mathbb{A}_I \cdot \bar{\boldsymbol{\varepsilon}} + \mathbf{e}_I \theta \quad (I = 1, \ldots, N), \quad \boldsymbol{\varepsilon}_{\mathrm{m}} = \mathbb{A}_{\mathrm{m}} \cdot \bar{\boldsymbol{\varepsilon}} + \mathbf{e}_{\mathrm{m}} \theta \,. \tag{7}$$

When the mechanical strain localization tensors $\mathbb{A}_I$, $\mathbb{A}_{\mathrm{m}}$ and the thermal strain localization tensors of the second order: $\mathbf{e}_I$, $\mathbf{e}_{\mathrm{m}}$ are known, the set of relations (1–7) enables one to find the mean stresses and strains per each family and the matrix, as well as macroscopic stress or strain, depending on which of these two quantities is prescribed by the boundary conditions.

Following [25], and notation introduced in [8], it can be demonstrated that for the multi-family variant of the interaction model, the mechanical strain localization tensors for the families and the matrix are found from the following set of fourth-order equations:

$$\sum_{K=1}^{N} \mathbb{M}^{IK} \mathbb{A}_K = \mathbb{I}, \quad I = 1, 2, \ldots, N \tag{8}$$

and

$$\mathbb{A}_{\mathrm{m}} = \frac{1}{1 - f_{\mathrm{i}}} \left(\mathbb{I} - f_{\mathrm{i}} \mathbb{A}_{\mathrm{i}} \right), \tag{9}$$

where $\mathbb{A}_{\mathrm{i}}$ is specified by (6). The fourth-order tensors $\mathbb{M}^{IK}$ are specified as

$$\mathbb{M}^{IK} = \begin{cases} \mathbb{I} + \left((1 - f_K)\mathbb{P}_0 - \bar{\boldsymbol{\Gamma}}^{IK} \right) (\mathbb{C}_{\mathrm{i}} - \mathbb{C}_{\mathrm{m}}) & \text{for} \quad K = I \\ -\left(\bar{\boldsymbol{\Gamma}}^{IK} + f_K \mathbb{P}_0 \right) (\mathbb{C}_{\mathrm{i}} - \mathbb{C}_{\mathrm{m}}) & \text{for} \quad K \neq I. \end{cases} \tag{10}$$

The tensor $\mathbb{P}_0$ is the so-called polarisation tensor for a spherical inclusion immersed in the matrix material (see Eq. (15)). The tensors $\bar{\boldsymbol{\Gamma}}^{IK}$ convey averaged mutual interaction between inclusions belonging to two families I and K. They are obtained by summing the interactions between each inclusion pair I and j such that I denotes the reference inclusion of the family I *in the elementary cube (i.e. RUC)*, while inclusion j belongs to the family K and is one of N_K inclusions which are obtained by periodic expansion of the elementary cube, namely:

$$\bar{\boldsymbol{\Gamma}}^{IK} = \begin{cases} \sum_{j=2}^{N_K} \boldsymbol{\Gamma}^{Ij} & \text{for} \quad K = I \\ \sum_{j=1}^{N_K} \boldsymbol{\Gamma}^{Ij} & \text{for} \quad K \neq I. \end{cases} \tag{11}$$

For isotropic properties of the matrix and the spherical shape of inclusions, tensors $\boldsymbol{\Gamma}^{Ij}$ are specified in the Appendix A of [8] (see also [22]). Note that for the multi-family case, a and b in these formulas are now the radii of inclusions belonging to the family I and K, respectively ($a = b$ in the present analysis of inclusions of equal sizes) and R is a distance between the reference inclusion of the family I *in the elementary cube (i.e. RUC)* and the inclusion j of family K in the cluster.

The second-order thermal strain localization tensors $\mathbf{e}_I$ ($I = 1, 2, \ldots, N$) for the thermoelastic problem are found from the related set of N second-order tensor equations

$$\sum_{I=1}^{N} \mathbb{M}^{IK} \cdot \mathbf{e}_K = \bar{\mathbf{w}}^I, \quad K = 1, 2, \ldots, N \tag{12}$$

and

$$\mathbf{e}_{\mathrm{m}} = -\frac{1}{1 - f_{\mathrm{i}}} \sum_{I=1}^{N} f_I \mathbf{e}_I \,. \tag{13}$$

The fourth-order tensors $\mathbb{M}^{IK}$ are specified above, while the second-order tensors $\bar{\mathbf{w}}^I$ are specified as:

$$\bar{\mathbf{w}}^I = \sum_{L=1}^{N} \mathbf{w}^{IL} \text{ where } \mathbf{w}^{IL} = \begin{cases} \left((1 - f_L)\mathbb{P}_0 - \bar{\boldsymbol{\Gamma}}^{IL} \right) \cdot (\boldsymbol{\beta}_{\mathrm{i}} - \boldsymbol{\beta}_{\mathrm{m}}) & \text{for } L = I \\ -\left(\bar{\boldsymbol{\Gamma}}^{IL} + f_L \mathbb{P}_0 \right) \cdot (\boldsymbol{\beta}_{\mathrm{i}} - \boldsymbol{\beta}_{\mathrm{m}}) & \text{for } L \neq I \end{cases} \tag{14}$$

with $\bar{\mathbf{\Gamma}}^{IL}$ and $\mathbb{P}_0$ specified before.

Let us observe that the solution of the set of tensorial equations (8) and (12) requires an extension of the classical procedures used to solve linear equations. The extended Gauss elimination procedure is provided in the Appendix A.

3 Numerical full-field model

Mean-field estimates obtained by the cluster model are compared below with the results of numerical homogenization performed using the Finite Element Method (FEM), for random microstructures with non-overlaping spherical particles of equal radius. The FE analyses were performed in the AceFEM environment [37], with the structural FE meshes for the RUCs generated using NetGen [38]. Thirty *RUCs with 50 randomly-placed inclusions* were generated and analyzed for each of the volume fractions of inclusions f_i equal to 0.1, 0.2, 0.3, 0.4 and 0.5. RUCs within each group differed in their normalized mean nearest-neighbour distances $\bar{\lambda}/(2a)$, ranging from around 0.035 to 0.815 for $f_\mathrm{i} = 0.1$, from 0.008 to 0.454 for $f_\mathrm{i} = 0.2$, from 0.004 to 0.280 for $f_\mathrm{i} = 0.3$, from 0.003 to 0.162 for $f_\mathrm{i} = 0.4$ and from 0.001 to 0.079 for $f_\mathrm{i} = 0.5$. Selected RUCs for $f_\mathrm{i} = 0.2$—one with the second lowest and one with the highest $\bar{\lambda}/(2a)$—are shown in Fig. 2(a,b), and analogous ones for $f_\mathrm{i} = 0.4$ in Fig. 2(c,d). In the present paper, the mean nearest-neighbour distance $\bar{\lambda}$ has been calculated by finding a mean of the distances λ_I between the outer surface of particle I and the surface of its nearest neighbour. Such a distance is computed first as a minimum of distances l_{IJ} between the centre points of inclusion I and any other inclusion J in the RUC (taking into account periodicity of the microstructure) and subtracting $2a$, where a is the particle radius, the same for all particles. Consequently, if particle I is in contact with its nearest neighbour then $\lambda_I = 0$.

All RUCs were generated in a $1 \times 1 \times 1$ cube. The cube was assumed to be a periodic cell, with the inclusions crossing the boundary copied periodically to the opposite sides of the cube. The random placement of inclusions was performed using Yade [39], a Discrete Element Method (DEM) system. The adopted approach followed the one used in [40] and exploited the dynamics of spherical elastic particles. To have greater control over the mean nearest-neighbour distance of the generated microstructures—in particular to facilitate obtaining values of $\bar{\lambda}/(2a)$ near the lowest and highest ends of the spectrum—some adaptations were introduced. They were described in detail in [19]. In summary, the particles were first placed in an enlarged periodic cell of size $2 \times 2 \times 2$ using Yade's built-in Random Sequential Addition algorithm and assigned random velocities. This step presents no problems even when generating dense final packings, since the target volume fraction of particles in the unit $(1 \times 1 \times 1)$ cell dilutes to one-eight of its value in the enlarged cell. Next, the cell gradually contracted to unit size with simultaneous gas-like dynamic mixing of the particles, after which the system was left to stabilize in the presence of numerical damping. Finally, a snapshot of the system was taken, with the centers of particles assumed to be the centers of inclusions of the composite. To enforce an upper limit on the resulting mean nearest-neighbour distance, two-particle "molecules" were inserted into the enlarged cell and simulated instead of single particles. They underwent similar mixing during compression of the cell, resembling dynamics of gas molecules, with the distance between the two particles of each molecule preserved during the movement. In this way, if the particles in each pair were a distance d apart, then $\bar{\lambda} \leqslant d$ in the final configuration. To enforce a lower limit on the mean nearest-neighbour distance, the particles' diameters were initially increased by d. This ensured that in the final configuration $\bar{\lambda} \geqslant d$. Adjustments were also made in each case to accommodate the minute overlaps of the elastic particles which might remain in the final configuration.

We remark that the particle packing (or clustering) can be described by different parameters or distribution functions, see for example [3,35,41]. The choice of mean nearest-neighbour distance $\bar{\lambda}$ as a primary variable in the presented analyses is dictated by two facts. Firstly, contrary to radial distribution or exclusion probability functions, which could be alternatively used, it is a scalar parameter. This parameter can be directly controlled, at least to some degree, by the RUC generation procedures and is easily accessible for the generated microstructures. Another scalar parameter which could be used is the relative volume fraction of clustered particles, used for example by [5], however, such a parameter is rather dedicated to the 'globular' clusters, and would be difficult to assess for any microstructure. Secondly, the existing literature widely uses $\bar{\lambda}$ in the particle packing description indicating it as a parameter which controls stress and strain distribution in the individual particles (e.g. [32]). This parameter was also used in the formulations of some of the advanced mean field models like the MRP approach mentioned in the introduction. Thus, by using this parameter, the presented results are placed in a broader literature context. Nonetheless, we would like to emphasize that the mean nearest-neighbour distance is in fact used only to collectively present results for the considered set of RUCs

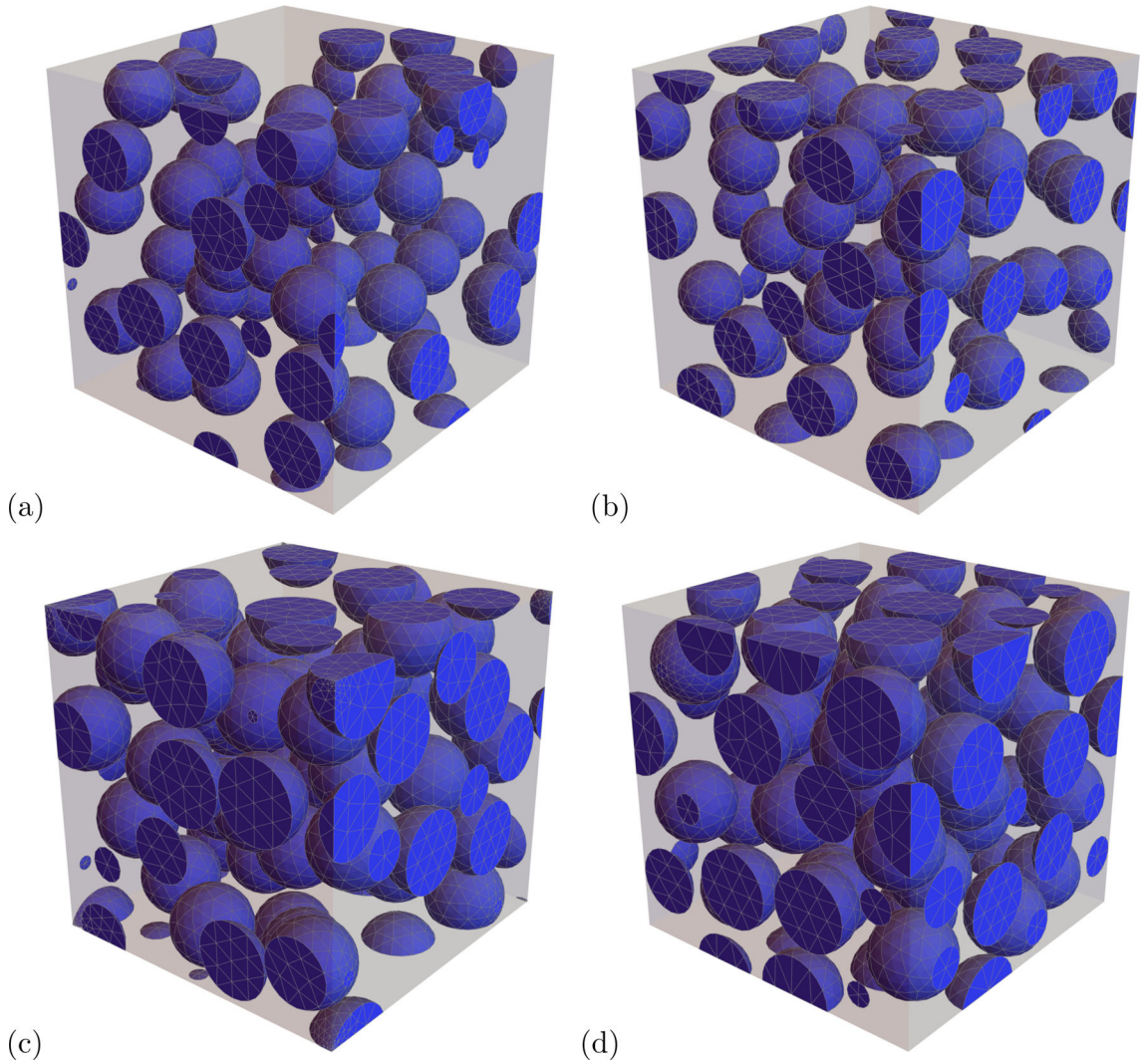

Fig. 2 Periodic RUCs with 50 randomly-placed inclusions with the FE mesh shown only for the inclusions:**(a)** $f_\mathrm{i} = 0.2$, $\bar{\lambda}/(2a) = 0.018$, **(b)** $f_\mathrm{i} = 0.2$, $\bar{\lambda}/(2a) = 0.454$, **(c)** $f_\mathrm{i} = 0.4$, $\bar{\lambda}/(2a) = 0.005$, and **(d)** $f_\mathrm{i} = 0.4$, $\bar{\lambda}/(2a) = 0.162$

and meaningfully differentiate between them. As such it has not been used in the cluster model formulation, which takes into account all the information about the spatial distribution of inclusions in the RUC, so the spatial distribution of particles is exactly the same in the numerical and analytical models. The geometrical data for all considered microstructures are openly available in the data set linked at the end of the article.

For the purpose of performing FEM analyses, the generated RUCs were meshed using tetrahedral, 10 node, second-order finite elements. The final mesh contained between 20 and 50 thousand elements, depending on the volume fraction of inclusions and the particular random geometry. The adopted mesh density guaranteed sufficient accuracy of results at a moderate computational cost, compared with more time-consuming computations based on finer meshes. Each of the geometrically-periodic samples was subjected to micro-periodic displacement boundary conditions to assure periodicity of deformation.

4 Results

Three types of FEM simulations were performed to validate the predictions of the cluster model. The first one aimed at determining effective elastic parameters of the composites. Six independent deformation tests were performed for each microstructure, with the global deformation tensor $\bar{\boldsymbol{\varepsilon}}$ of the RUC having just one nonzero

Table 1 The material parameters of $AlSi_{12}$, Al_2O_3 and SiC [36] used in simulations: the Young's modulus E, the Poisson's ratio ν and the thermal expansion coefficient α

Material	E[GPa]	ν	$\alpha[10^{-6}/°C]$
$AlSi_{12}$	70	0.35	23.7
Al_2O_3	380	0.22	6.5
SiC	410	0.15	4.0

component in each test, namely $\bar{\varepsilon}_{11} = \delta$ or $\bar{\varepsilon}_{22} = \delta$ or $\bar{\varepsilon}_{33} = \delta$ or $2\bar{\varepsilon}_{12} = \delta$ or $2\bar{\varepsilon}_{13} = \delta$ or $2\bar{\varepsilon}_{23} = \delta$, with $\delta = 10^{-4}$ in all tests. From the average stresses in the RUC obtained in the six tests, the full effective stiffness tensor $\bar{\mathbb{C}}$ of the composite was determined in each case. This allowed further calculation of the values of the effective bulk and shear moduli of the composite, $\bar{K}$ and $\bar{G}$, respectively, computed for an isotropic material whose stiffness tensor was the closest to $\bar{\mathbb{C}}$ in terms of Euclidean distance. The second type of tests were thermal expansion simulations, aimed at determining the average thermal expansion coefficient $\bar{\alpha}$ for each composite. They consisted in assigning a static, uniform temperature increase $\Delta T = 10°C$ to the entire RUC and allowing its unconstrained expansion. The value of $\bar{\alpha}$ was determined from the overall volumetric strain $\bar{\varepsilon}_{kk}$ of the RUC. The third type of tests were uniaxial stress simulations, performed by assigning $\bar{\varepsilon}_{33} = \delta$ as the global deformation of a given RUC in the direction x_3, and allowing free deformation of the RUC in the remaining directions. In all tests, average strains and stresses in all inclusions and in the matrix were recorded.

Four types of composites were numerically investigated. The first one was made of $AlSi_{12}$ matrix reinforced with Al_2O_3 inclusions, the second of $AlSi_{12}$ matrix with SiC inclusions, the third one was $AlSi_{12}$ matrix with voids, and the fourth one—$AlSi_{12}$ matrix with very hard inclusions. The values of the elastic thermomechanical parameters of the real constituent materials are presented in Table 1. The voids were simulated as weakened matrix material, having 10^{-4} the stiffness of $AlSi_{12}$, instead of being modeled as actual empty space. This was to facilitate the gathering of results, particularly of void deformations, which could be gleaned in the present scheme from the deformation of the FE mesh filling the voids. The hard inclusions, in turn, were assumed to have 10^4 the stiffness of $AlSi_{12}$ (with the same Poisson's ratio), and 10^{-4} the thermal expansion coefficient of $AlSi_{12}$.

A number of representative results of the performed calculations are presented in Figs. 3–10, as well as in Tables 2–11. In the most disadvantageous cases among all conducted tests, the discrepancy between the cluster model and FEM results for the effective bulk modulus, $\bar{K}$, and shear modulus, $\bar{G}$, was up to around 2% and 8%, respectively, for the composites with Al_2O_3 and SiC inclusions, and up to around 9% and 12%, respectively, for the $AlSi_{12}$ matrix with voids. A similar discrepancy for the effective thermal expansion coefficient, $\bar{\alpha}$, was below 2%. In the extreme case of hard inclusions at $f_i = 50\%$ and very low $\bar{\lambda}/(2a)$, the mismatch reached 22% for $\bar{K}$ and as much as 50% for $\bar{G}$. Overall, the mismatch between the cluster model and FEM was observed to significantly increase with increasing f_i for all of the above-mentioned quantities, especially at $f_i \geqslant 30\%$, with decreasing $\bar{\lambda}/(2a)$ and increasing contrast between phases. Therefore, the agreement between the methods for "regular" composites with moderate volume fractions of inclusions was significantly better than indicated by the percentages above.

Example results for $f_i = 20\%$ and 40%, and all 30 random RUCs with different values of the packing parameter $\bar{\lambda}/(2a)$, are shown in Figs. 3–6. Overall, as mentioned earlier, the discrepancy between the cluster model and FEM results is clearly greater for $f_i = 40\%$ (c,d) than for $f_i = 20\%$ (a,b) in all figures. Fig. 3 shows the values of $\bar{K}$ (a,c) and $\bar{G}$ (b,d) for the $AlSi_{12}$-Al_2O_3 composite. It can be seen that the predicted values of both quantities decrease with increasing $\bar{\lambda}/(2a)$, as is the difference between the cluster model and FEM results. Generally, the FEM results decrease with increasing $\bar{\lambda}/(2a)$ faster than the cluster model results, displaying greater sensitivity to particle packing. It should be remarked that the $AlSi_{12}$-SiC composite, results for which are not shown in the figures, behaves analogously to the $AlSi_{12}$-Al_2O_3 one. Similar results for $AlSi_{12}$ with voids are shown in Fig. 4. Here, the values of $\bar{K}$ and $\bar{G}$ increase with increasing $\bar{\lambda}/(2a)$, with the cluster model results being again less dependent on the packing parameter. The results for hard inclusions in the $AlSi_{12}$ matrix are presented in Fig. 5. The character of the plots is similar to the ones for the composites with Al_2O_3 (and SiC) inclusions, but here the extreme contrast between the phase properties makes the cluster model and FEM results deviate from each other much further. Finally, in Fig. 6, one can see the estimates of $\bar{\alpha}$ for the $AlSi_{12}$-Al_2O_3 (a,c) and $AlSi_{12}$-SiC (b,d) composites over the same packing-parameter range. The FEM results display yet again greater dependence on the packing parameter.

Table 2 Cluster model / FEM estimates of the effective bulk modulus, $\bar{K}_C$ / $\bar{K}_F$, shear modulus, $\bar{G}_C$ / $\bar{G}_F$, and thermal expansion coefficient, $\bar{\alpha}_C$ / $\bar{\alpha}_F$, for microstructures with the second lowest and highest values of $\bar{\lambda}/(2a)$ for $f_i = 10, 20, 30, 40, 50\%$. As a reference, the estimates by the Mori-Tanaka (MT) model are provided. Composite: $AlSi_{12}$ matrix with Al_2O_3 inclusions

f_i[%]	$\bar{\lambda}/(2a)$	$\bar{K}_C$[GPa]	$\bar{K}_F$[GPa]	$\bar{G}_C$[GPa]	$\bar{G}_F$[GPa]	$\bar{\alpha}_C[10^{-6}/°C]$	$\bar{\alpha}_F[10^{-6}/°C]$
10	0.041	84.60	84.68	30.22	30.45	21.59	21.56
	0.815	84.56	84.58	30.15	30.28	21.60	21.59
	MT	84.56		30.14		21.60	
20	0.018	92.31	92.57	35.23	35.89	19.57	19.51
	0.454	92.21	92.26	35.11	35.47	19.60	19.59
	MT	92.21		35.04		19.60	
30	0.009	101.05	101.54	41.07	42.45	17.66	17.57
	0.280	100.92	101.04	40.86	41.81	17.69	17.66
	MT	100.91		40.80		17.69	
40	0.005	111.09	112.12	48.10	50.61	15.84	15.68
	0.162	110.94	111.19	47.77	49.57	15.86	15.82
	MT	110.89		47.68		15.87	
50	0.005	122.73	124.49	56.52	61.17	14.10	13.88
	0.079	122.57	123.29	56.25	59.47	14.12	14.02
	MT	122.47		56.04		14.13	

Table 3 Cluster model / FEM estimates of the effective bulk modulus, $\bar{K}_C$ / $\bar{K}_F$, shear modulus, $\bar{G}_C$ / $\bar{G}_F$, and thermal expansion coefficient, $\bar{\alpha}_C$ / $\bar{\alpha}_F$, for microstructures with the second lowest and highest values of $\bar{\lambda}/(2a)$ for $f_i = 10, 20, 30, 40, 50\%$. As a reference, the estimates by the Mori-Tanaka (MT) model are provided. Composite: $AlSi_{12}$ matrix with SiC inclusions

f_i[%]	$\bar{\lambda}/(2a)$	$\bar{K}_C$[GPa]	$\bar{K}_F$[GPa]	$\bar{G}_C$[GPa]	$\bar{G}_F$[GPa]	$\bar{\alpha}_C[10^{-6}/°C]$	$\bar{\alpha}_F[10^{-6}/°C]$
10	0.041	83.86	83.93	30.44	30.70	21.32	21.30
	0.815	83.83	83.85	30.36	30.5	21.34	21.33
	MT	83.83		30.35		21.34	
20	0.018	90.65	90.87	35.76	36.52	19.05	18.98
	0.454	90.57	90.61	35.62	36.03	19.07	19.06
	MT	90.57		35.54		19.06	
30	0.009	98.24	98.64	42.00	43.63	16.88	16.78
	0.28	98.13	98.23	41.76	42.86	16.91	16.88
	MT	98.12		41.69		16.91	
40	0.005	106.80	107.63	49.62	52.61	14.80	14.63
	0.162	106.68	106.88	49.23	51.36	14.83	14.78
	MT	106.65		49.12		14.81	
50	0.005	116.55	117.85	58.84	63.88	12.81	12.57
	0.079	116.43	116.99	58.52	62.41	12.83	12.72
	MT	116.35		58.26		12.85	

The results obtained for $f_i = 10, 30, 50\%$, which are not presented in figures, behave analogously to those in Figs. 3–6 for $f_i = 20, 40\%$. One can observe that, in general, the estimates of $\bar{G}$ obtained by both methods are more scattered than those for $\bar{K}$ and $\bar{\alpha}$. This demonstrates a greater dependence of $\bar{G}$ and lesser dependence of $\bar{K}$ on other spatial characteristics of composite microstructures besides the packing parameter. The nature of the dependence seems to be captured by the cluster model, in the sense that whenever there is an uptick or downtick in the FEM-computed value of $\bar{G}$ about its local mean, the cluster model estimate usually follows in the same direction.

Numerical values of the effective parameters $\bar{K}$, $\bar{G}$ and $\bar{\alpha}$ computed using the cluster model and FEM for two RUCs with extreme values of $\bar{\lambda}/(2a)$ for each $f_i = 10, 20, 30, 40, 50\%$ are collected in Table 2 (for the $AlSi_{12}$-Al_2O_3 composite), Table 3 (for the $AlSi_{12}$-SiC composite), Table 4 (for $AlSi_{12}$ with voids), and Table 5 (for the $AlSi_{12}$-hard-inclusions composite). In the tables, the Mori-Tanaka (MT) estimates are additionally provided for comparison. It can be seen that the MT values closely match the cluster model predictions obtained for the RUCs with the highest values of the packing parameter $\bar{\lambda}/(2a)$—namely those in which inclusions/voids are more "evenly" distributed in the matrix. In other words, the cluster model results converge towards the MT estimates as $\bar{\lambda}/(2a)$ increases.

Tables 6–11 and Figs. 7–10 present selected results regarding stresses/strains obtained by the cluster model and FEM in 50 individual inclusions/voids and in the matrix of two RUCs with extreme values of $\bar{\lambda}/(2a)$ for $f_i = 10, 20, 30, 40, 50\%$. Table 6 contains the results for the σ_{33} stresses in the $AlSi_{12}$-Al_2O_3 composite

Table 4 Cluster model / FEM estimates of the effective bulk modulus, $\bar{K}_C$ / $\bar{K}_F$, and shear modulus, $\bar{G}_C$ / $\bar{G}_F$, for microstructures with the second lowest and highest values of $\bar{\lambda}/(2a)$ for $f_i = 10, 20, 30, 40, 50\%$. As a reference, the estimates by the Mori-Tanaka (MT) model are provided. Composite: $AlSi_{12}$ matrix with voids

f_i[%]	$\bar{\lambda}/(2a)$	$\bar{K}_C$[GPa]	$\bar{K}_F$[GPa]	$\bar{G}_C$[GPa]	$\bar{G}_F$[GPa]
10	0.041	56.8	56.73	21.43	21.44
	0.815	57.14	57.39	21.49	21.60
	MT	57.15		21.49	
20	0.018	42.36	41.90	17.56	17.42
	0.454	42.89	43.18	17.72	17.82
	MT	42.92		17.71	
30	0.009	31.98	31.3	14.23	13.92
	0.28	32.47	32.76	14.39	14.38
	MT	32.51		14.44	
40	0.005	24.06	22.90	11.35	10.74
	0.162	24.47	24.45	11.49	11.17
	MT	24.57		11.59	
50	0.005	17.87	16.55	8.87	7.99
	0.079	18.13	17.65	8.97	8.28
	MT	18.31		9.08	

Table 5 Cluster model / FEM estimates of the effective bulk modulus, $\bar{K}_C$ / $\bar{K}_F$, shear modulus, $\bar{G}_C$ / $\bar{G}_F$, and thermal expansion coefficient, $\bar{\alpha}_C$ / $\bar{\alpha}_F$, for microstructures with the second lowest and highest values of $\bar{\lambda}/(2a)$ for $f_i = 10, 20, 30, 40, 50\%$. As a reference, the estimates by the Mori-Tanaka (MT) model are provided. Composite: $AlSi_{12}$ matrix with hard inclusions

f_i[%]	$\bar{\lambda}/(2a)$	$\bar{K}_C$[GPa]	$\bar{K}_F$[GPa]	$\bar{G}_C$[GPa]	$\bar{G}_F$[GPa]	$\bar{\alpha}_C$[10^{-6}/°C]	$\bar{\alpha}_F$[10^{-6}/°C]
10	0.041	90.48	91.12	32.41	33.33	20.37	20.23
	0.815	90.26	90.35	32.19	32.5	20.42	20.4
	MT	90.26		32.17		20.42	
20	0.018	106.43	109.2	40.65	44.08	17.32	16.89
	0.454	105.89	106.11	40.17	41.22	17.41	17.37
	MT	105.9		39.97		17.41	
30	0.009	126.86	132.97	51.09	59.49	14.53	13.87
	0.28	126.00	126.73	50.24	53.64	14.63	14.55
	MT	125.9		49.99		14.64	
40	0.005	154.27	171.18	65.42	82.76	11.96	10.91
	0.162	153.01	155.23	63.85	72.33	12.05	11.88
	MT	152.7		63.36		12.08	
50	0.005	192.96	236.02	84.91	133.70	9.55	7.85
	0.079	191.17	200.76	83.36	105.54	9.64	9.18
	MT	190.1		82.07		9.70	

under uniaxial stress in the x_3 direction at the global strain $\bar{\varepsilon}_{33} = 10^{-4}$. It can be seen that while average stresses in the matrix predicted by both methods agree quite well, even for higher f_i, the average values over all inclusions differ by up to around 10%, with FEM predicting higher stresses. The added estimates by the Mori-Tanaka method agree quite well with the cluster model predictions. It can also be noticed that, firstly, the standard deviations of mean values of σ_{33} in all 50 inclusions, following from both the cluster model and FEM results, are higher for the microstructures with lower $\bar{\lambda}/(2a)$ than for those with higher ones. This indicates, as can be expected, that the less evenly the inclusions are distributed in a composite, the greater is the variation of stresses among the inclusions. Secondly, the standard deviations computed by both methods generally increase with increasing f_i. This also simultaneously shows that the cluster model is able to capture those effects. The computed mean values of σ_{33} in all inclusions for $f_i = 20\%$ and 40% are presented in Fig. 7, where the difference in the stress variation between inclusions for RUCs with a small (a,c) and large (b,d) values of $\bar{\lambda}/(2a)$ is clearly seen.

Table 7 provides analogous results, under uniaxial stress conditions, for stresses σ_{33} in the $AlSi_{12}$-SiC composite, which exhibit similar trends to the ones for $AlSi_{12}$-Al_2O_3 described above. Table 8, in turn, summarizes the results for the case of $AlSi_{12}$ with voids. Here, the ε_{33} strains are presented instead of stresses which vanish in the voids. A good agreement between the cluster model and FEM results for the matrix is observed when $f_i \leqslant 30\%$, after which the predictions begin to diverge more significantly. For the voids, the relative difference in the mean values of ε_{33} obtained by the cluster model and FEM tends to be smaller

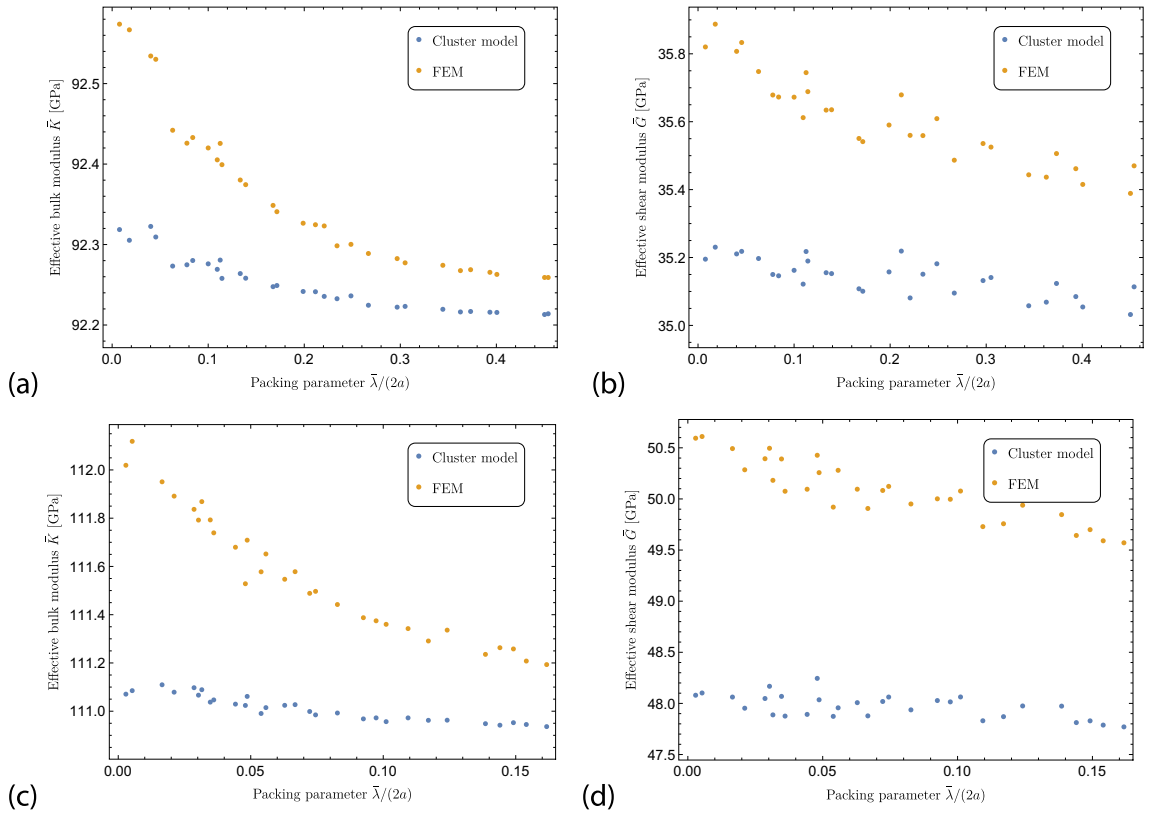

Fig. 3 Cluster model and FEM estimations of **(a,c)** the effective bulk modulus $\bar{K}$ and **(b,d)** the shear modulus $\bar{G}$ of the $AlSi_{12}$ matrix reinforced with Al_2O_3 particles (Tab.1) vs. the packing parameter $\bar{\lambda}/(2a)$. The RUC contains 50 inclusions occupying a volume fraction $f_i = 20\%$ (a,b) and $f_i = 40\%$ (c,d)

than that for σ_{33} in the composites with Al_2O_3 or SiC inclusions, reaching about 4.5%. As previously, the Mori-Tanaka estimates match closely the results for the RUCs with high values of the packing parameter. The dispersion of the mean values of ε_{33} among the voids, as measured by the standard deviation, is much greater for the RUCs with lower values of $\bar{\lambda}/(2a)$. This is also demonstrated more comprehensively in Fig. 8 for the case of $f_i = 20\%$ and 40%.

The results provided in Table 9 showcase the performance of the cluster model versus FEM regarding the extreme phase-contrast case of $AlSi_{12}$ matrix with hard inclusions under the same uniaxial stress conditions as above. It can be seen that while the average stresses σ_{33} in the matrix predicted by the cluster model and FEM match relatively well up to $f_i = 40\%$, the predicted mean values in inclusions diverge rapidly with increasing f_i, reaching around 77% relative error for $f_i = 50\%$ and low $\bar{\lambda}/(2a)$. The increasing dispersion of results between individual inclusions with increasing f_i and decreasing $\bar{\lambda}/(2a)$, predicted by both the cluster model and FEM, is also clearly visible both in Table 9 and in Fig. 9. While the FEM results may carry numerical errors of their own, this extreme case highlights the limitations of the predictive capabilities of the cluster model when dealing with large phase contrasts.

The final two Tables 10 and 11 list results obtained for the $AlSi_{12}$-Al_2O_3 and $AlSi_{12}$-SiC composites, respectively, in the unconstrained thermal expansion tests under a uniform temperature increase $\Delta T = 10°C$. Since the tests themselves have an isotropic character, hydrostatic stresses $\sigma_{kk}/3$ in the matrix and inclusions were analysed. The data obtained for both composites have similar features. There is a noticeable discrepancy between the cluster model and FEM results both for the inclusions and for the matrix, up to around 25% in the case of $f_i = 50\%$. Generally, as already noted before, the mismatch between the methods increases with increasing f_i and decreasing $\bar{\lambda}/(2a)$, meaning that denser and more closely-packed composites are more difficult to accurately model using the cluster scheme. The cluster model can be also observed to consistently underestimate the hydrostatic stresses, in terms of their absolute values, with respect to the FEM results. The greater dispersion of mean values in individual inclusions for the RUCs with lower values of $\bar{\lambda}/(2a)$ is yet

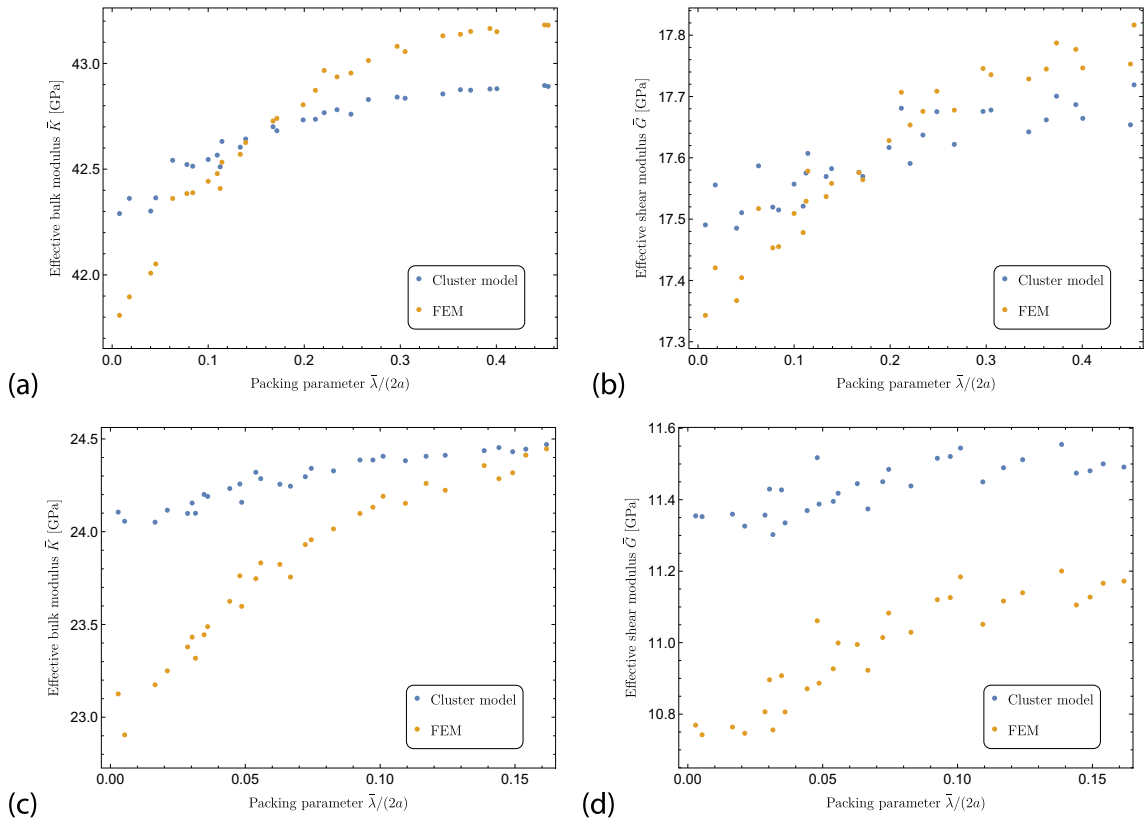

Fig. 4 Cluster model and FEM estimations of **(a,c)** the effective bulk modulus $\bar{K}$ and **(b,d)**the shear modulus $\bar{G}$ of the $AlSi_{12}$ matrix with voids (Tab.1) vs. the packing parameter $\bar{\lambda}/(2a)$. The RUC contains 50 voids occupying a volume fraction $f_i = 20\%$ **(a,b)**and $f_i = 40\%$ (c,d)

again apparent in Tables 10–11 and in Fig. 10 for the case of SiC inclusions at the $f_i = 20\%$ (a,b) and 40% (c,d) volume fraction.

The last remark about the results for individual inclusions is that the distributions of mean stresses or strains in all inclusions/voids obtained by the cluster model and FEM have similar shapes, as can be seen in Figs. 7–10. In other words, in some respects similarly to the case of effective values of $\bar{G}$ discussed earlier, if the mean stress or strain in one inclusion is greater than in another one according to FEM, then it is usually also greater according to the cluster model. This shows that the cluster model tends to correctly reflect the variability of the mean stresses or strains in individual inclusions/voids.

5 Conclusion

In the paper, efficient computational procedures for the multi-family variant of the cluster model were proposed. A broad verification of the method for three composites and a porous matrix with random inhomogeneity distribution has been performed by comparing the results of the analytical model with outcomes of numerical homogenization. To our best knowledge, a cluster model has not been yet applied and verified in the present context.

Analysis of the effect of packing on the overall thermoelastic properties and local response of particulate composites has been performed. In agreement with previous experimental and numerical studies we observed that while clustering has minimal influence on the overall elastic properties, it leads to a greater dispersion of mean fields between particles. The overall elastic stiffness increased only slightly with decreasing mean nearest-neighbour distance between inclusions, while at the same time such a change in the microstructure substantially affected the standard deviation of mean stresses for individual inclusions in the representative unit cells. Very good agreement between the mean-field model predictions and FEM results, both concerning the overall properties and estimates of local mean strains and stresses for individual inclusions, has been demonstrated up

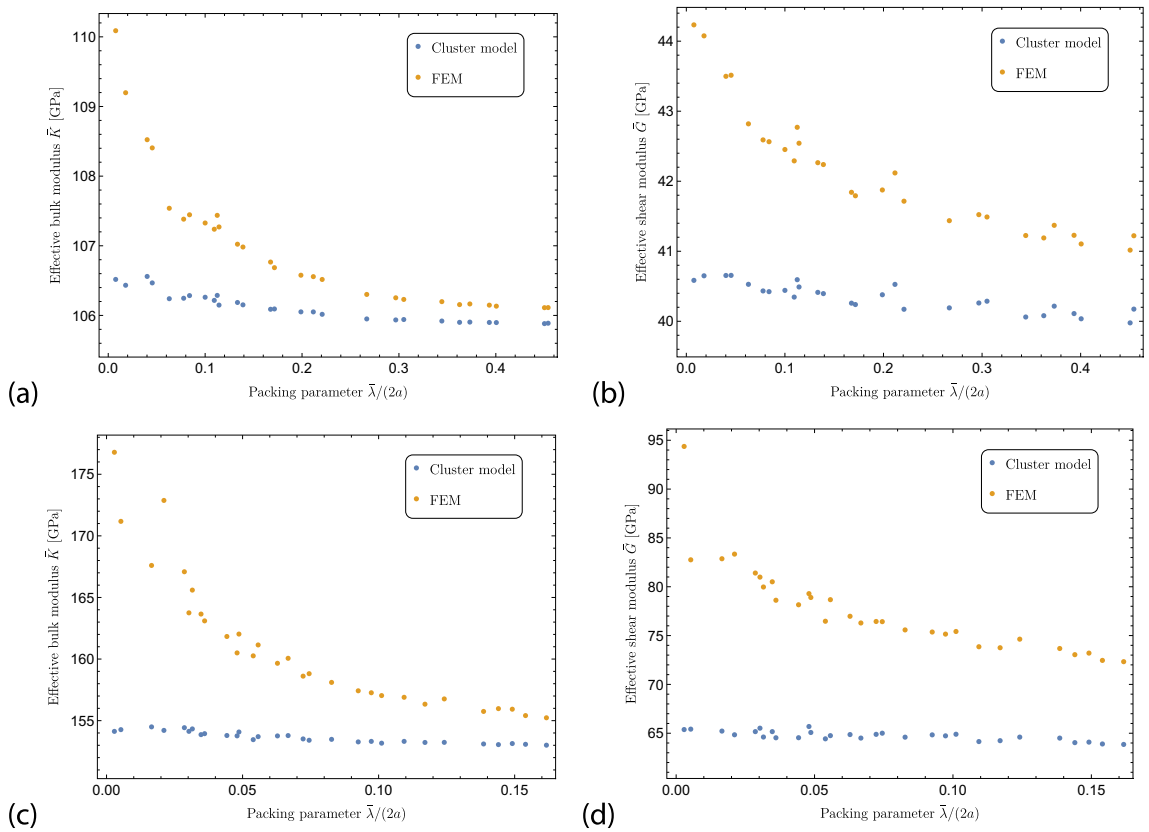

Fig. 5 Cluster model and FEM estimations of **(a,c)** the effective bulk modulus $\bar{K}$ and (b,d) the shear modulus $\bar{G}$ of the $AlSi_{12}$ matrix with hard inclusions (Tab.1) vs. the packing parameter $\bar{\lambda}/(2a)$. The RUC contains 50 inclusions occupying a volume fraction $f_i = 20\%$ (a,b) and $f_i = 40\%$ (c,d)

Table 6 Cluster model / FEM estimates of the σ_{33} stress: mean in all inclusions, σ_{33}^{iC} / σ_{33}^{iF}, standard deviation of means in individual inclusions: $\hat{\sigma}_{33}^{iC}$ / $\hat{\sigma}_{33}^{iF}$, and mean in the matrix: σ_{33}^{mC} / σ_{33}^{mF}, for microstructures with the second lowest and highest values of $\bar{\lambda}/(2a)$ for $f_i = 10, 20, 30, 40, 50\%$. Composite: $AlSi_{12}$ matrix with Al_2O_3 inclusions. Uniaxial stress along x_3 at global strain $\bar{\varepsilon}_{33} = 10^{-4}$.

f_i[%]	$\bar{\lambda}/(2a)$	σ_{33}^{iC}[MPa]	$\hat{\sigma}_{33}^{iC}$[MPa]	σ_{33}^{iF}[MPa]	$\hat{\sigma}_{33}^{iF}$[MPa]	σ_{33}^{mC}[MPa]	σ_{33}^{mF}[MPa]
10	0.041	12.42	1.06	12.95	1.30	7.61	7.62
	0.815	12.39	0.16	12.69	0.17	7.61	7.61
	MT	12.33				7.61	
20	0.018	13.73	1.18	14.57	1.54	8.30	8.29
	0.454	13.50	0.29	13.93	0.33	8.31	8.31
	MT	13.41				8.31	
30	0.009	14.86	1.18	16.04	1.59	9.11	9.08
	0.280	14.76	0.45	15.52	0.55	9.12	9.12
	MT	14.67				9.24	
40	0.005	16.12	1.07	17.60	1.38	10.14	10.08
	0.162	16.32	0.51	17.45	0.68	10.06	10.03
	MT	16.16				10.08	
50	0.005	18.22	1.44	20.47	2.11	11.20	10.98
	0.079	18.02	0.80	19.59	1.10	11.22	11.10
	MT	17.95				11.23	

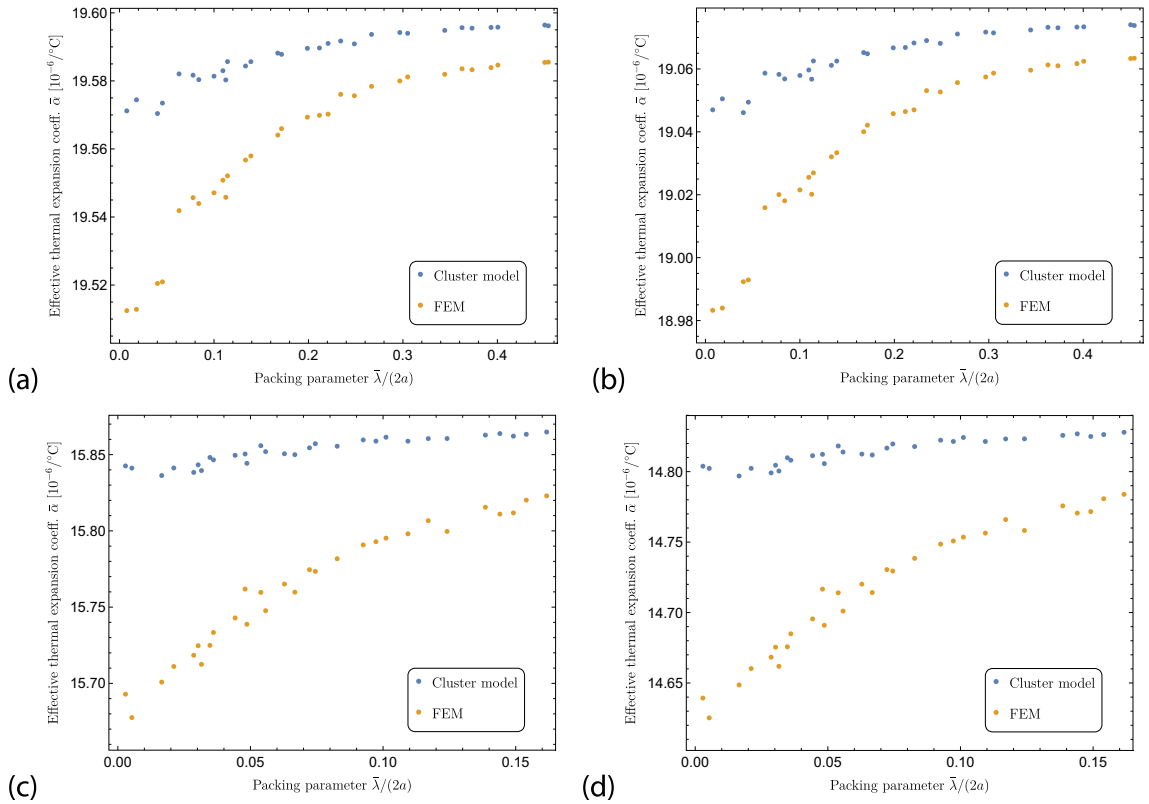

Fig. 6 Cluster model and FEM estimations of the effective thermal expansion coefficient $\bar{\alpha}$ of the $AlSi_{12}$ matrix reinforced with **(a,c)** Al_2O_3 and **(b,d)**SiC particles (Tab. 1) vs. the packing parameter $\bar{\lambda}/(2a)$. The RUC contains 50 inclusions occupying a volume fraction $f_i = 20\%$ (a,b) and $f_i = 40\%$ (c,d)

Table 7 Cluster model / FEM estimates of the σ_{33} stress: mean in all inclusions, σ_{33}^{iC} / σ_{33}^{iF}, standard deviation of means in individual inclusions: $\hat{\sigma}_{33}^{iC}$ / $\hat{\sigma}_{33}^{iF}$, and mean in the matrix: σ_{33}^{mC} / σ_{33}^{mF}, for microstructures with the second lowest and highest values of $\bar{\lambda}/(2a)$ for $f_i = 10, 20, 30, 40, 50\%$. Composite: $AlSi_{12}$ matrix with SiC inclusions. Uniaxial stress along x_3 at global strain $\bar{\varepsilon}_{33} = 10^{-4}$

f_i[%]	$\bar{\lambda}/(2a)$	σ_{33}^{iC}[MPa]	$\hat{\sigma}_{33}^{iC}$[MPa]	σ_{33}^{iF}[MPa]	$\hat{\sigma}_{33}^{iF}$[MPa]	σ_{33}^{mC}[MPa]	σ_{33}^{mF}[MPa]
10	0.041	12.60	1.11	13.17	1.38	7.64	7.65
	0.815	12.55	0.17	12.88	0.18	7.64	7.64
	MT	12.50				7.63	
20	0.018	13.98	1.25	14.91	1.65	8.36	8.36
	0.454	13.73	0.30	14.20	0.35	8.38	8.38
	MT	13.64				8.38	
30	0.009	15.18	1.25	16.51	1.71	9.23	9.20
	0.280	15.06	0.48	15.91	0.59	9.24	9.24
	MT	14.97				9.24	
40	0.005	16.53	1.13	18.2	1.49	10.32	10.28
	0.162	16.72	0.54	18.00	0.73	10.24	10.22
	MT	16.56				10.25	
50	0.005	18.78	1.53	21.19	2.20	11.47	11.31
	0.079	18.56	0.85	20.35	1.20	11.47	11.38
	MT	18.47				11.48	

Table 8 Cluster model / FEM estimates of the ε_{33} strain: mean in all inclusions, $\varepsilon_{33}^{\mathrm{iC}}$ / $\varepsilon_{33}^{\mathrm{iF}}$, standard deviation of means in individual inclusions: $\hat{\varepsilon}_{33}^{\mathrm{iC}}$ / $\hat{\varepsilon}_{33}^{\mathrm{iF}}$, and mean in the matrix: $\varepsilon_{33}^{\mathrm{mC}}$ / $\varepsilon_{33}^{\mathrm{mF}}$, for microstructures with the second lowest and highest values of $\bar{\lambda}/(2a)$ for $f_{\mathrm{i}} = 10, 20, 30, 40, 50\%$. Composite: $AlSi_{12}$ matrix with voids. Uniaxial stress along x_3 at global strain $\bar{\varepsilon}_{33} = 10^{-4}$

f_{i}[%]	$\bar{\lambda}/(2a)$	$\varepsilon_{33}^{\mathrm{iC}}[10^{-4}]$	$\hat{\varepsilon}_{33}^{\mathrm{iC}}[10^{-4}]$	$\varepsilon_{33}^{\mathrm{iF}}[10^{-4}]$	$\hat{\varepsilon}_{33}^{\mathrm{iF}}[10^{-4}]$	$\varepsilon_{33}^{\mathrm{mC}}[10^{-4}]$	$\varepsilon_{33}^{\mathrm{mF}}[10^{-4}]$
10	0.041	1.857	0.177	1.852	0.168	0.905	0.905
	0.815	1.810	0.032	1.773	0.030	0.910	0.914
	MT	1.815				0.909	
20	0.018	1.687	0.159	1.714	0.154	0.828	0.822
	0.454	1.662	0.046	1.645	0.042	0.835	0.839
	MT	1.665				0.834	
30	0.009	1.565	0.163	1.609	0.170	0.758	0.740
	0.280	1.540	0.060	1.540	0.055	0.768	0.769
	MT	1.537				0.770	
40	0.005	1.467	0.142	1.527	0.152	0.689	0.649
	0.162	1.428	0.061	1.457	0.064	0.715	0.696
	MT	1.427				0.715	
50	0.005	1.348	0.127	1.413	0.145	0.652	0.588
	0.079	1.343	0.086	1.389	0.096	0.657	0.612
	MT	1.332				0.668	

Table 9 Cluster model / FEM estimates of the σ_{33} stress: mean in all inclusions, $\sigma_{33}^{\mathrm{iC}}$ / $\sigma_{33}^{\mathrm{iF}}$, standard deviation of means in individual inclusions: $\hat{\sigma}_{33}^{\mathrm{iC}}$ / $\hat{\sigma}_{33}^{\mathrm{iF}}$, and mean in the matrix: $\sigma_{33}^{\mathrm{mC}}$ / $\sigma_{33}^{\mathrm{mF}}$, for microstructures with the second lowest and highest values of $\bar{\lambda}/(2a)$ for $f_{\mathrm{i}} = 10, 20, 30, 40, 50\%$. Composite: $AlSi_{12}$ matrix with hard inclusions. Uniaxial stress along x_3 at global strain $\bar{\varepsilon}_{33} = 10^{-4}$

f_{i}[%]	$\bar{\lambda}/(2a)$	$\sigma_{33}^{\mathrm{iC}}$[MPa]	$\hat{\sigma}_{33}^{\mathrm{iC}}$[MPa]	$\sigma_{33}^{\mathrm{iF}}$[MPa]	$\hat{\sigma}_{33}^{\mathrm{iF}}$[MPa]	$\sigma_{33}^{\mathrm{mC}}$[MPa]	$\sigma_{33}^{\mathrm{mF}}$[MPa]
10	0.041	15.45	2.01	17.24	3.33	7.92	7.96
	0.815	15.24	0.29	15.85	0.31	7.91	7.92
	MT	15.13				7.90	
20	0.018	18.11	2.50	22.03	5.18	9.03	9.13
	0.454	17.39	0.56	18.45	0.70	9.03	9.08
	MT	17.18				9.02	
30	0.009	20.50	2.55	26.58	5.75	10.45	10.69
	0.280	20.05	0.95	22.36	1.34	10.46	10.62
	MT	0.770				10.44	
40	0.005	23.54	2.48	32.82	7.41	12.46	12.50
	0.162	23.76	1.19	28.33	2.07	12.33	12.70
	MT	23.27				12.32	
50	0.005	29.55	4.02	52.62	14.71	15.03	16.16
	0.079	28.60	2.08	37.79	4.51	14.96	15.72
	MT	28.11				14.93	

to 30-40% of particle volume fraction of not-too-rigid inclusions. The validity regime is somewhat extended for the case of soft or void-like inclusions, however, the quality of estimates strongly deteriorates for increased volume fractions, approaching impenetrability limit for a given microstructure, especially in the case of hard or rigid inclusions. This validity range is consistent with the previous findings related to the particulate composites with a regular particle arrangement [8]. These limitations arise from an increasing violation of the cluster model assumption of uniform stress and strain fields within the inclusions. As far as we are aware, a mean-field model for thermoelastic metal matrix composites with comparable computational efficiency and predictive capabilities regarding the response of individual inclusions, depending on their location in the representative volume is not available in the existing literature.

The proposed approach is planned to be used in studying damage development in composite materials as it enables assessment of different thresholds of damage initiation depending on the spatial distribution of randomly-placed particles in a representative composite volume. In the present research, the particles were assumed to be spherical and of equal size, while the considered examples differed in the volume fraction of inclusions and their mean nearest-neighbour distances. In the future, microstructures with different inhomogeneity sizes or ellipsoidal particle shapes are intended to be studied.

Table 10 Cluster model / FEM estimates of the hydrostatic stress $\sigma_h = \sigma_{kk}/3$: mean in all inclusions, σ_h^{iC} / σ_h^{iF}, standard deviation of means in individual inclusions: $\hat{\sigma}_h^{iC}$ / $\hat{\sigma}_h^{iF}$, and mean in the matrix: σ_h^{mC} / σ_h^{mF}, for microstructures with the second lowest and highest values of $\bar{\lambda}/(2a)$ for $f_i = 10, 20, 30, 40, 50\%$. Composite: $AlSi_{12}$ matrix with Al_2O_3 inclusions. Unconstrained thermal expansion under a uniform temperature increase $\Delta T = 10°C$.

f_i[%]	$\bar{\lambda}/(2a)$	σ_h^{iC}[MPa]	$\hat{\sigma}_h^{iC}$[MPa]	σ_h^{iF}[MPa]	$\hat{\sigma}_h^{iF}$[MPa]	σ_h^{mC}[MPa]	σ_h^{mF}[MPa]
10	0.041	13.99	0.19	14.91	0.31	-1.55	-1.65
	0.815	13.59	0.02	13.88	0.06	-1.51	-1.54
	MT	13.58				-1.51	
20	0.018	12.19	0.32	13.37	0.58	-3.05	-3.34
	0.454	11.80	0.07	12.08	0.09	-2.95	-3.01
	MT	11.78				-2.94	
30	0.009	10.39	0.39	11.61	0.79	-4.45	-4.96
	0.280	10.10	0.11	10.46	0.12	-4.33	-4.47
	MT	10.07				-4.31	
40	0.005	8.70	0.51	10.24	1.02	-5.80	-6.80
	0.162	8.49	0.22	8.95	0.28	-5.66	-5.95
	MT	8.43				-5.62	
50	0.005	7.12	0.59	8.74	1.09	-7.12	-8.64
	0.079	6.97	0.35	7.74	0.53	-6.97	-7.71
	MT	6.87				-6.87	

Table 11 Cluster model / FEM estimates of the hydrostatic stress $\sigma_h = \sigma_{kk}/3$: mean in all inclusions, σ_h^{iC} / σ_h^{iF}, standard deviation of means in individual inclusions: $\hat{\sigma}_h^{iC}$ / $\hat{\sigma}_h^{iF}$, and mean in the matrix: σ_h^{mC} / σ_h^{mF}, for microstructures with the second lowest and highest values of $\bar{\lambda}/(2a)$ for $f_i = 10, 20, 30, 40, 50\%$. Composite: $AlSi_{12}$ matrix with SiC inclusions. Unconstrained thermal expansion under a uniform temperature increase $\Delta T = 10°C$

f_i[%]	$\bar{\lambda}/(2a)$	σ_h^{iC}[MPa]	$\hat{\sigma}_h^{iC}$[MPa]	σ_h^{iF}[MPa]	$\hat{\sigma}_h^{iF}$[MPa]	σ_h^{mC}[MPa]	σ_h^{mF}[MPa]
10	0.041	15.75	0.22	16.82	0.38	-1.75	-1.87
	0.815	15.28	0.02	15.61	0.07	-1.70	-1.73
	MT	15.27				-1.70	
20	0.018	13.76	0.37	15.16	0.69	-3.44	-3.78
	0.454	13.31	0.08	13.62	0.11	-3.33	-3.40
	MT	13.28				-3.32	
30	0.009	11.75	0.46	13.20	0.95	-5.04	-5.64
	0.280	11.41	0.13	11.83	0.14	-4.89	-5.06
	MT	11.37				-4.87	
40	0.005	9.87	0.60	11.68	1.23	-6.58	-7.76
	0.162	9.62	0.26	10.15	0.34	-6.41	-6.75
	MT	9.55				-6.36	
50	0.005	8.09	0.69	10.00	1.31	-8.09	-9.98
	0.079	7.91	0.41	8.83	0.63	-7.91	-8.80
	MT	7.79				-7.79	

Acknowledgements K.K.-G. acknowledges the financial support provided to the research by the European Union's Research and Innovation Program Horizon Europe under the Grant Agreement No. 101086342 – HORIZON-MSCA-2021-SE-01 Project DIAGONAL (Ductility and fracture toughness analysis of Functionally Graded Materials), co-founded by the Polish Ministry of Science and Higher Education under the program "International Projects Co-financed". P.H. and M.M. acknowledge the support of the National Science Centre through the project 2021/41/B/ST8/03345 within which procedures for computational homogenization of representative unit cells with random distribution of inhomogeneities have been developed.

Author Contribution PH: software development, calculations, results visualisation; writing—original draft; writing—review & editing. MM: software development; data curation; investigation; writing—review & editing. KK-G (corresponding author):

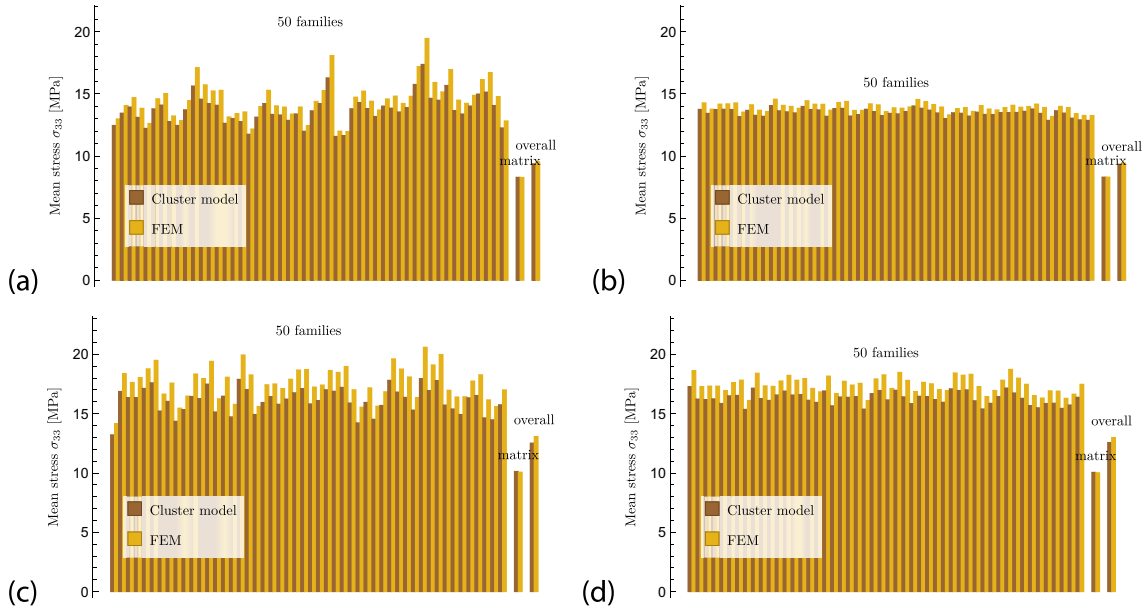

Fig. 7 Mean stress σ_{33} in all 50 Al_2O_3 inclusions, in the $AlSi_{12}$ matrix and in the entire RUC, obtained by the cluster model and FEM for the microstructures in Fig. 2**(a–d)**, respectively, under uniaxial stress of the RUC along x_3 at global strain $\bar{\varepsilon}_{33} = 10^{-4}$

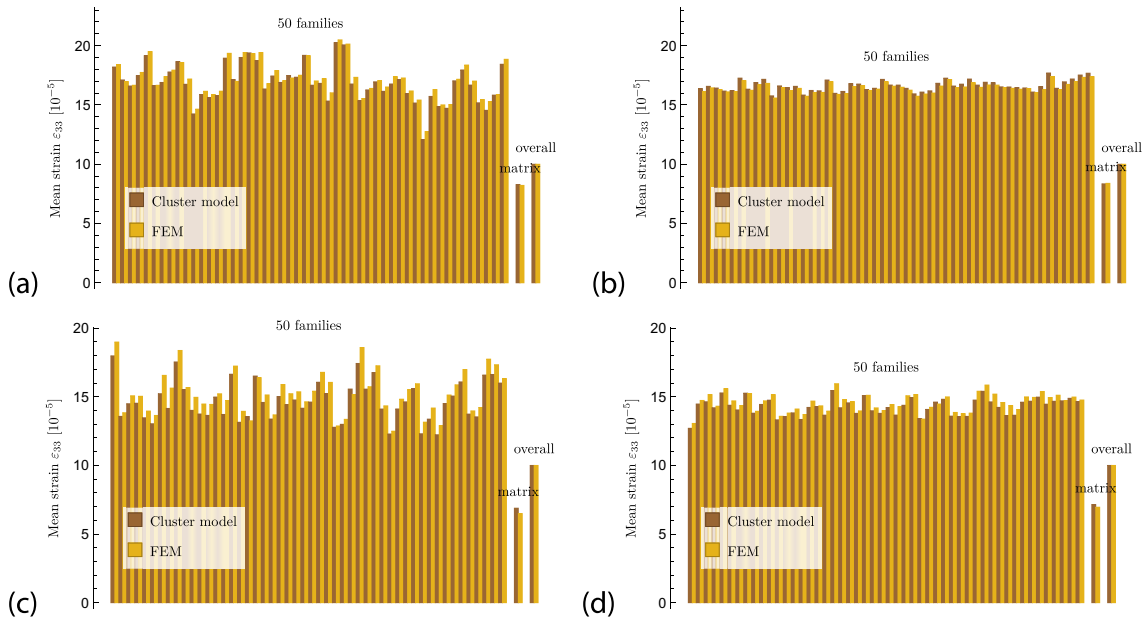

Fig. 8 Mean strain ε_{33} in all 50 voids, in the $AlSi_{12}$ matrix and in the entire RUC, obtained by the cluster model and FEM for the microstructures in Fig. 2**(a–d)**, respectively, under uniaxial stress of the RUC along x_3 at global strain $\bar{\varepsilon}_{33} = 10^{-4}$

conceptualization; funding acquisition; methodology; software development; supervision; validation; visualisation; writing—original draft; writing—review & editing.

Data Availibility The authors declare that the data supporting the findings of this study are freely available at RePOD (Repository of Open Data) using the link https://doi.org/10.18150/IRZUEX.

Declarations

Conflicts of Interest The authors declare no competing interests.

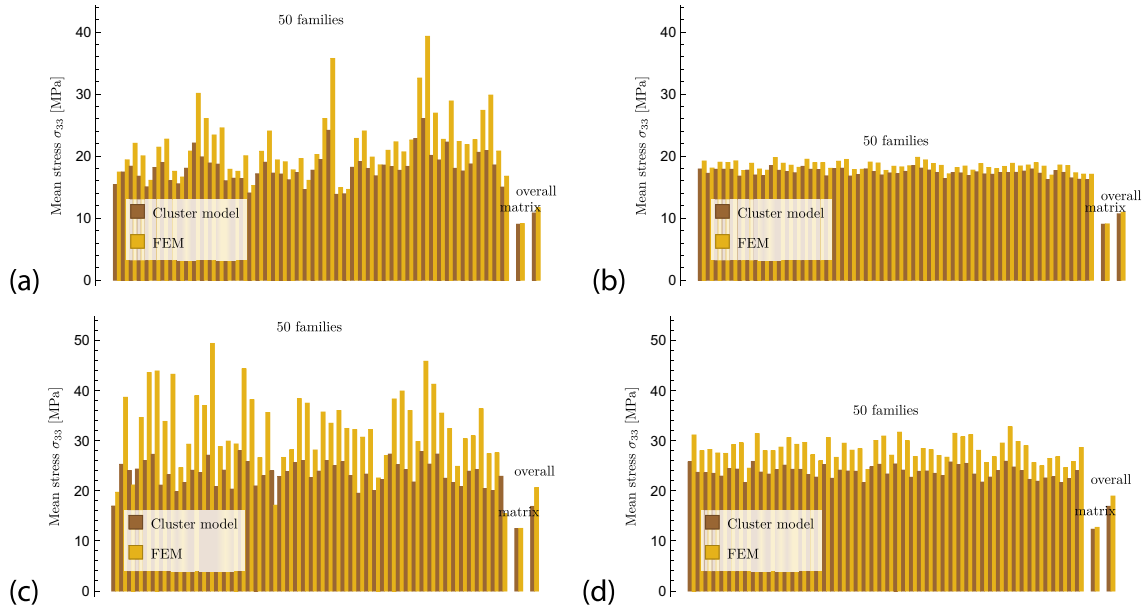

Fig. 9 Mean stress σ_{33} in all 50 hard inclusions, in the $AlSi_{12}$ matrix and in the entire RUC, obtained by the cluster model and FEM for the microstructures in Fig. 2**(a–d)**, respectively, under uniaxial stress of the RUC along x_3 at global strain $\bar{\varepsilon}_{33} = 10^{-4}$.

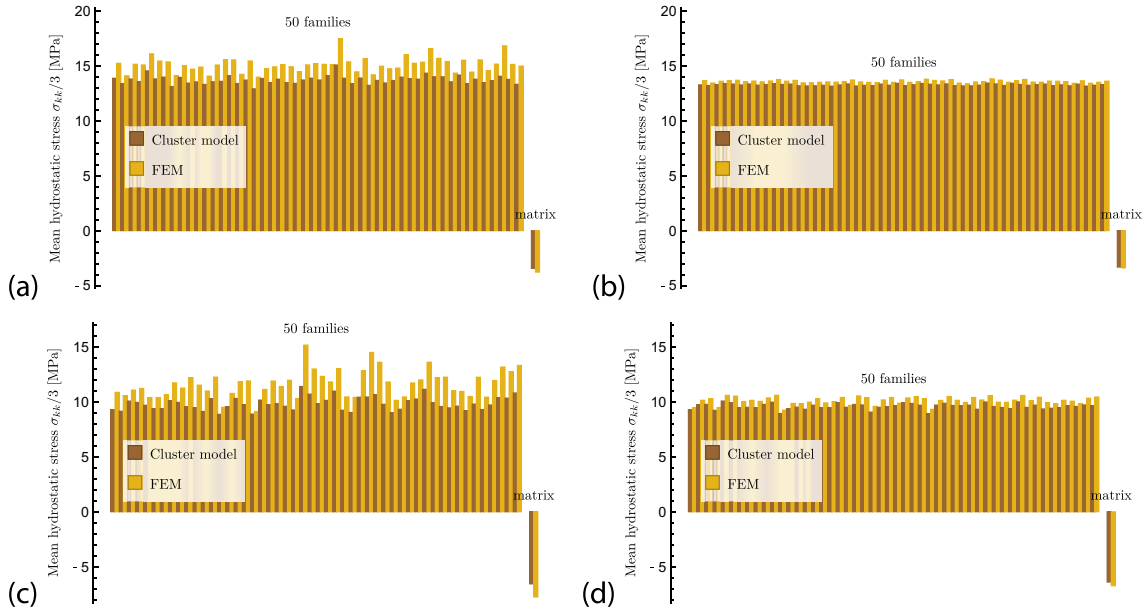

Fig. 10 Mean hydrostatic stress $\sigma_{kk}/3$ in all 50 SiC inclusions and in the $AlSi_{12}$ matrix, obtained by the cluster model and FEM for the microstructures in Fig. 2**(a–d)**, respectively, for unconstrained thermal expansion of the RUC under uniform temperature increase $\Delta T = 10°C$

A Computational algorithm for the multi-family variant of the cluster model

In order to find the effective properties (4) and (5) of the composite with the use of the cluster interaction model, the averaged interaction tensors (11) need to be calculated for each pair I and K of families. These tensors are required to specify the localization tensors $\mathbb{A}_K$.

The computational algorithm, which is followed to compute effective thermoelastic properties and localization tensors for the interaction cluster model in the case of a particulate two-phase composite with spherical inclusions, is composed of the following steps (isotropic properties of the matrix phase are assumed):

Step 1: Input data are read, including

- local properties of the two phases: $\mathbb{C}_r$, $\boldsymbol{\beta}_r$ ($r = \mathrm{m}, \mathrm{i}$),
- the set of locations (x_I, y_I, z_I) and radii r_I of particles ($I = 1, \ldots, N$) in the elementary cubic volume $1 \times 1 \times 1$ of the composite,
- the cluster size R_c.

Step 2: The averaged interaction tensors (11) are calculated for each pair (I, K) of inclusion families. Details of the algorithm for finding the tensor $\bar{\boldsymbol{\Gamma}}^{IK}$ for a given pair of families are discussed below. The polarisation tensor $\mathbb{P}_0$ is calculated for the isotropic matrix material by the formula

$$\mathbb{P}_0 = \frac{1 - 2\nu_\mathrm{m}}{6\mu_\mathrm{m}(1 - \nu_\mathrm{m})}\mathbb{I}_P + \frac{2(4 - 5\nu_\mathrm{m})}{15\mu_\mathrm{m}}\mathbb{I}_D\,, \tag{15}$$

where μ_m and ν_m are the shear modulus and Poisson's ratio of the isotropic matrix material, and $\mathbb{I}_P$ and $\mathbb{I}_D$ are orthogonal projectors to the subspaces of hydrostatic and deviatoric second-order tensors, respectively.

Step 3: The fourth-order tensors $\mathbb{M}^{IK}$ and the second-order tensors $\mathbf{w}^K$ ($I, K = 1, \ldots, N$) are calculated using the formulas (10) and (14).

Step 4: The sets of fourth-order tensorial equations (8) and second-order tensorial equations (12) are solved using the extended Gauss elimination procedure discussed below. By solving these sets of equations, the fourth-order localization tensors $\mathbb{A}_I$ and the second-order tensors $\mathbf{e}_I$ are found. Next, $\mathbf{A}_\mathrm{m}$ and $\mathbf{e}_\mathrm{m}$ are found using (9) and (13).

Step 5: The effective elastic stiffness tensor $\bar{\mathbb{C}}$ and thermal stress tensor $\bar{\boldsymbol{\beta}}$ are calculated using relations (4) and (5).

It should be noted that despite the assumed random distribution of particles the effective properties are not perfectly isotropic due to the finite number of particles in the representative unit cell.

The computationally efficient procedure for finding the $\bar{\boldsymbol{\Gamma}}^{IK}$ tensor for a given pair (I, K) of families in step 2 of the algorithm above proceeds as follows:

Step 2.1: Input data are read, including

- elastic constants of the isotropic matrix: μ_m, ν_m,
- locations (x_I, y_I, z_I) and (x_K, y_K, z_K) as well as radii r_I and r_K of two particles in the elementary unit volume $1 \times 1 \times 1$ of the composite,
- the cluster size R_c .

Step 2.2: If $I = K$, by translating the inclusion I to the frame origin and repeating it periodically in each of the three directions, the regular cubic (RC) arrangement of particles is obtained. Using this observation, the closed form relations derived in [8] are used to compute the $\bar{\boldsymbol{\Gamma}}^{II}$ tensor.

Step 2.3: If $I < K$,

- the pair of inclusions is translated in space so that inclusion I is placed at the frame origin: $(x_I^*, y_I^*, z_I^*) = (0, 0, 0)$, while inclusion K is moved to the position $(x_K^*, y_K^*, z_K^*) = (x_K - x_I, y_K - y_I, z_K - z_I)$,
- inclusion K is periodically repeated in space in three directions to form an infinite set of inclusions $(x_j^{*(K)}, y_j^{*(K)}, z_j^{*(K)})$ ($j = 1, \ldots, \infty$) belonging to the family K,
- to form a cluster, inclusions $j = 1, \ldots, N_c$ of the family K which satisfy the condition $(x_j^{*(K)})^2 + (y_j^{*(K)})^2 + (z_j^{*(K)})^2 \le R_c^2$ are selected,
- the tensor $\bar{\boldsymbol{\Gamma}}^{IK}$ is calculated by summing the tensors $\boldsymbol{\Gamma}^{Ij}$. The latter are calculated using the relations (B.1-B.6) in [8] in which R is the distance between inclusion I and j-th inclusion of the family K, so that $R = \sqrt{(x_K^{*(j)})^2 + (y_K^{*(j)})^2 + (z_K^{*(j)})^2}$, components of the unit vector $\mathbf{n}$ are $n_k = (x_K^{*(j)}/R, y_K^{*(j)}/R, z_K^{*(j)}/R)$, while a and b are radii r_I and r_K, respectively.

Step 2.4: If $I > K$, the symmetry property of the tensor $\bar{\boldsymbol{\Gamma}}^{IK}$ is used [23], namely (no summation over I and K)

$$r_I^3 \bar{\boldsymbol{\Gamma}}^{IK} = r_K^3 \bar{\boldsymbol{\Gamma}}^{KI}\,.$$

The extended Gauss elimination procedure solves the set of the tensorial equations of the form $[\mathbf{M}].[\mathbf{X}] = [\mathbf{b}]$, where $[\mathbf{M}]$ is a known $N \times N$ matrix of second-order tensors $\mathbf{M}^{IK}$ $(I, K = 1, \ldots, N)$ in $E^k \otimes E^k$ tensorial space, $[\mathbf{X}]$ and $[\mathbf{b}]$ are column vectors of N unknown and known tensors $\mathbf{X}_K$ and $\mathbf{b}^I$, respectively, in $E^k \otimes E^l$ tensorial space. When applied to equation set (8), $k = l = 6$, as the fourth-order tensors $\mathbb{M}^{IK}$, $\mathbb{A}_K$ and $\mathbb{I}$ are written as second-order tensors in six-dimensional space (see [42]). When applied to (12), $k = 6$ while $l = 1$, as the second-order tensors $\mathbf{e}^K$ and $\mathbf{w}_I$ are written as vectors in six-dimensional space. The first stage of the algorithm is aimed to transform the original set of equations into $[\mathbf{M}_*].[\mathbf{X}] = [\mathbf{b}_*]$, in which in the matrix $[\mathbf{M}_*]$ the diagonal tensorial components are identity tensors: $\mathbf{M}_*^{II} = \mathbf{I}$, while components $\mathbf{M}_*^{IK}$ for which $I > K$ are equal to $\mathbf{0}$. Next, the solution for $[\mathbf{X}]$ is found by substitution, starting from the element $\mathbf{X}_N = \mathbf{b}_*^N$. The detailed algorithm proceeds as follows:

1. The sought variables $[\mathbf{M}_*]$ and $[\mathbf{b}_*]$ are preset to $[\mathbf{0}]$, while iterative variables $[\mathbf{M}_{\text{trial}}]$ and $[\mathbf{b}_{\text{trial}}]$ are preset to $[\mathbf{M}]$ and $[\mathbf{b}]$.
2. For $I = 1, \ldots, N-1$ we perform the steps:
   - calculate (no summation over I)
   $$\mathbf{b}_*^I = (\mathbf{M}_{\text{trial}}^{II})^{-1}\mathbf{b}_{\text{trial}}^I$$
   - for $K = I, \ldots, N$ calculate
   $$\mathbf{M}_*^{IK} = (\mathbf{M}_{\text{trial}}^{II})^{-1}(\mathbf{M}_{\text{trial}}^{IK})$$
   - replace $\mathbf{M}_{\text{trial}}^{IK}$ and $\mathbf{b}_{\text{trial}}^I$ with $\mathbf{M}_*^I$ and $\mathbf{b}_*^I$, respectively.
   - For $K = I+1, \ldots, N$ calculate
     - for $L = I+1, \ldots, N$ calculate
     $$\mathbf{M}_*^{KL} = \mathbf{M}_{\text{trial}}^{KL} - \mathbf{M}_{\text{trial}}^{KI}\mathbf{M}_{\text{trial}}^{IL}$$
     and replace $\mathbf{M}_{\text{trial}}^{KL} = \mathbf{M}_*^{KL}$,
     - calculate
     $$\mathbf{b}_*^K = \mathbf{b}_{\text{trial}}^K - \mathbf{M}_{\text{trial}}^{KI}\mathbf{b}_{\text{trial}}^I$$
     and replace $\mathbf{b}_{\text{trial}}^K = \mathbf{b}_*^K$.
3. Calculate $\mathbf{b}_*^N = (\mathbf{M}_{\text{trial}}^{NN})^{-1}\mathbf{b}_{\text{trial}}^N$.
4. Preset $[\mathbf{X}] = [\mathbf{0}]$
5. Set $\mathbf{X}_N = \mathbf{b}_*^N$
6. For $I = 1, \ldots, N-1$ calculate

$$\mathbf{X}_{N-I} = \mathbf{b}_*^{N-I} + \sum_{K=N-I+1}^{N} \mathbf{M}_*^{N-I,K}\mathbf{X}_K$$

Having found the effective thermoelastic properties, assuming some macroscopic stress tensor $\bar{\boldsymbol{\sigma}}$ or strain tensor $\bar{\boldsymbol{\varepsilon}}$ and temperature increase θ, the respective local quantities can be found. For example, mean strains and stresses in all particles in the representative unit cell for the uniaxial tension process in direction 1 up to tensile strain $\varepsilon_{11} = 0.01$, with no temperature change ($\theta = 0$), can be found assuming:

$$\bar{\boldsymbol{\sigma}} \sim \begin{bmatrix} \Sigma & 0 & 0 \\ 0 & 0 & 0 \\ 0 & 0 & 0 \end{bmatrix} \quad \bar{\boldsymbol{\varepsilon}} \sim \begin{bmatrix} 0.01 & E_{12} & E_{13} \\ E_{12} & E_{22} & E_{23} \\ E_{13} & E_{23} & E_{33} \end{bmatrix}$$

Next, using the overall relation (3) in the reduced form $\bar{\boldsymbol{\sigma}} = \bar{\mathbb{C}} \cdot \bar{\boldsymbol{\varepsilon}}$, we find the six unknowns: Σ, E_{22}, E_{33}, E_{12}, E_{13}, E_{23}. After finding the overall strain $\bar{\boldsymbol{\varepsilon}}$, mean strains and stresses for each inclusion in the RUC are found by the localization relation and local constitutive law: $\boldsymbol{\varepsilon}_I = \mathbb{A}_I \cdot \bar{\boldsymbol{\varepsilon}}$, $\boldsymbol{\sigma}_I = \mathbb{C}_{\text{i}} \cdot \boldsymbol{\varepsilon}_I$. If one considers a cooling or heating process with a temperature change θ under zero external stress, thermal strains and stresses in each inclusion and the matrix can be found assuming $\bar{\boldsymbol{\sigma}} = \mathbf{0}$ and solving first the overall relation $\bar{\mathbf{C}} \cdot \bar{\boldsymbol{\varepsilon}} - \bar{\boldsymbol{\beta}}\theta = \mathbf{0}$ for $\bar{\boldsymbol{\varepsilon}}$. Next, applying the localization relations (7) and the constitutive laws (1), one finds mean strains and stresses for each inclusion in the RUC and the matrix. Alternatively, in both cases, mean stresses in inclusions can be found by using stress localization tensors $\mathbb{B}_I$ and $\mathbf{s}_I$,

$$\mathbb{B}_I = \mathbb{C}_I\mathbb{A}_I\bar{\mathbb{C}}^{-1} \Rightarrow \boldsymbol{\sigma}_I = \mathbb{B}_I \cdot \bar{\boldsymbol{\sigma}} + \mathbf{s}_I\theta\,.$$

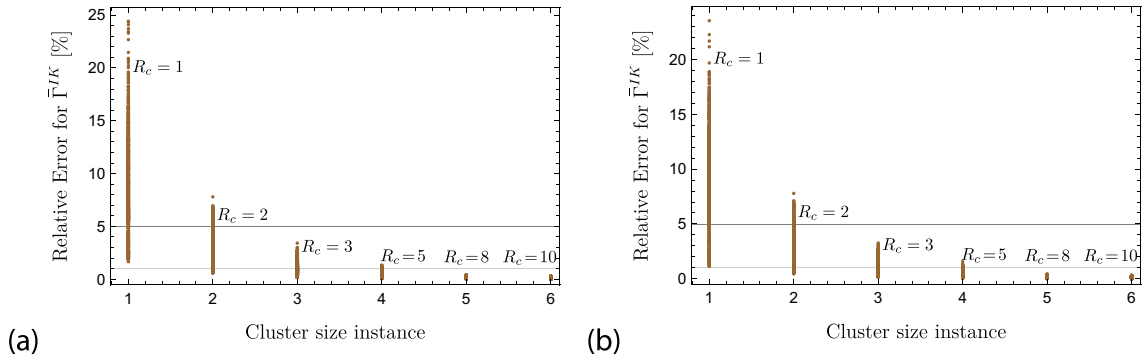

Fig. 11 Relative errors (16) for all the components of all $\bar{\mathbf{\Gamma}}^{KL}$, $(K, L = 1, \ldots, 50)$ for two selected microstructure realizations with (a) high $(\bar{\lambda}/(2R_i) = 0.28)$ and (b) low $(\bar{\lambda}/(2R_i) = 0.0043)$ mean minimum distance between the inclusions with a total volume fraction of 30%

B Convergence of the cluster model

As discussed above, the interaction cluster scheme requires one to define a cluster size R_c – a size of the domain for which direct interactions between a given pair of inclusions are accounted for (see Fig. 1). To establish a value which is large enough to obtain reliable results, we have calculated the averaged interaction tensors $\bar{\mathbf{\Gamma}}^{IK}$ for selected microstructure realizations increasing the cluster size from $R_c = 1$ to $R_c = 20$, assuming the representative unit volume to be a $1 \times 1 \times 1$ cube, and we have analyzed how the components Γ^{KL}_{ijkl} of these tensors change with an increasing cluster size. The relative error for a given component is defined as the following quantity

$$\varepsilon_{rel} = \frac{|\Gamma^{KL}_{ijkl}(R_c = 20) - \Gamma^{KL}_{ijkl}(R_c)|}{\Gamma^{KL}_{ijkl}(R_c = 20)} \times 100\%. \tag{16}$$

The results of the study for two microstructure realizations with a low and high mean minimum distance and the inclusion volume fraction of 30% are demonstrated in Fig. 11. It is seen that for the cluster size $R_c = 3$ the relative error drops below 5%, while for $R_c = 8$ it drops below 1%. Based on this outcome, in the calculations reported in this paper the cluster size $R_c = 10$ was assumed.

References

1. Fullwood, D.T., Niezgoda, S.R., Adams, B.L., Kalidindi, S.R.: Microstructure sensitive design for performance optimization. Pogress Mater. Sci. **55**, 477–562 (2010)
2. Kachanov, M., Sevostianov, I.: Micromechanics of Materials, with Applications. Springer (2018). https://doi.org/10.1007/978-3-319-76204-3
3. Torquato, S.: Random Heterogeneous Materials. Microstructure and Macroscopic Properties. Springer, New York (2002). https://doi.org/10.1007/978-1-4757-6355-3
4. Segurado, J., González, C., LLorca, J.: A numerical investigation of the effect of particle clustering on the mechanical properties of composites. Acta Mater. **51**(8), 2355–2369 (2003). https://doi.org/10.1016/S1359-6454(03)00043-0
5. Segurado, J., LLorca, J.: Computational micromechanics of composites: The effect of particle spatial distribution. Mech. Mater. **38**(8), 873–883 (2006). https://doi.org/10.1016/j.mechmat.2005.06.026
6. Ogierman, W., Pokorska, I., Burczyński, T.: Prediction of cement paste elastic properties via computational homogenization using digital microstructures. Int. J. Numer. Meth. Eng. **126**(24), 70200 (2025). https://doi.org/10.1002/nme.70200
7. Kachanov, M.: Effective properties of heterogeneous materials as functions of contrast between properties of constituents. Math. Mech. Solids **29**(12), 2476–2489 (2024). https://doi.org/10.1177/10812865221136236
8. Bieniek, K., Majewski, M., Hołobut, P., Kowalczyk-Gajewska, K.: Anisotropic effect of regular particle distribution in elastic-plastic composites: The modified tangent cluster model and numerical homogenization. Int. J. Eng. Sci. **203**, 104118 (2024). https://doi.org/10.1016/j.ijengsci.2024.104118
9. Vilchevskaya, E.N., Kushch, V.I., Kachanov, M., Sevostianov, I.: Effective properties of periodic composites: Irrelevance of one particle homogenization techniques. Mech. Mater. **159**, 103918 (2021). https://doi.org/10.1016/j.mechmat.2021.103918
10. Castañeda, P.P., Willis, J.R.: The effect of spatial distribution on the effective behavior of composite materials and cracked media. J. Mech. Phys. Solids **43**(12), 1919–1951 (1995). https://doi.org/10.1016/0022-5096(95)00058-Q
11. Hu, G.K., Weng, G.J.: The connections between the double-inclusion model and the Ponte Castaneda-Willis, Mori-Tanaka, and Kuster-Toksoz models. Mech. Mater. **32**(8), 495–503 (2000). https://doi.org/10.1016/S0167-6636(00)00015-6

12. Sevostianov, I.: On the shape of effective inclusion in the maxwell homogenization scheme for anisotropic elastic composites. Mech. Mater. **75**, 45–59 (2014). https://doi.org/10.1016/j.mechmat.2014.03.003
13. Sevostianov, I., Mogilevskaya, S.G., Kushch, V.I.: Maxwell's methodology of estimating effective properties: Alive and well. Int. J. Eng. Sci. **140**, 35–88 (2019). https://doi.org/10.1016/j.ijengsci.2019.05.001
14. Kushch, V.I.: Microstresses and effective elastic moduli of a solid reinforced by periodically distributed spheroidal particles. Int. J. Solids Struct. **34**(11), 1353–1366 (1997). https://doi.org/10.1016/S0020-7683(96)00078-9
15. Cohen, I.: Simple algebraic approximations for the effective elastic moduli of cubic arrays of spheres. J. Mech. Phys. Solids **52**(9), 2167–2183 (2004). https://doi.org/10.1016/j.jmps.2004.02.008
16. Schjødt-Thomsen, J., Pyrz, R.: Cubic inclusion arrangement: Effects on stress and effective properties. Comput. Mater. Sci. **34**(2), 129–139 (2005). https://doi.org/10.1016/j.commatsci.2004.12.061
17. Bornert, M., Stolz, C., Zaoui, A.: Morphologically representative pattern-based bounding in elasticity. J. Mech. Phys. Solids **44**(3), 307–331 (1996). https://doi.org/10.1016/0022-5096(95)00083-6
18. Marcadon, V., Herve, E., Zaoui, A.: Micromechanical modeling of packing and size effects in particulate composites. Int. J. Solids Struct. **44**(25), 8213–8228 (2007). https://doi.org/10.1016/j.ijsolstr.2007.06.008
19. Majewski, M., Kursa, M., Holobut, P., Kowalczyk-Gajewska, K.: Micromechanical and numerical analysis of packing and size effects in elastic particulate composites. Compos. B **124**, 158–174 (2017). https://doi.org/10.1016/j.compositesb.2017.05.004
20. Majewski, M., Holobut, P., Kursa, M., Kowalczyk-Gajewska, K.: Packing and size effects in elastic-plastic particulate composites: Micromechanical modelling and numerical verification. Int. J. Eng. Sci. **151**, 103271 (2020). https://doi.org/10.1016/j.ijengsci.2020.103271
21. Kowalczyk-Gajewska, K., Majewski, M., Mercier, S., Molinari, A.: Mean field interaction model accounting for the spatial distribution of inclusions in elastic-viscoplastic composites. Int. J. Solids Struct. **224**, 111040 (2021). https://doi.org/10.1016/j.ijsolstr.2021.111040
22. Molinari, A., El Mouden, M.: The problem of elastic inclusions at finite concentration. Int. J. Solids Structures **33**, 3131–3150 (1996)
23. Berveiller, M., Fassi-Fehri, O., Hihi, A.: The problem of two inclusions in an anisotropic medium. Int. J. Engrg. Sci. **25**, 691–709 (1987)
24. El Mouden, M., Cherkaoui, M., Molinari, A., Berveiller, M.: The overall elastic response of materials containing coated inclusions in a periodic array. Int. J. Eng. Sci. **36**(7), 813–829 (1998). https://doi.org/10.1016/S0020-7225(97)00111-0
25. El Mouden, M., Molinari, A.: Thermoelastic properties of composites containing ellipsoidal inhomogeneities. J. Therm. Stresses **23**, 233–255 (2000)
26. Mercier, S., Molinari, A., El Mouden, M.: Thermal conductivity of composite material with coated inclusions: Applications to tetragonal array of spheroids. J. Appl. Phys. **87**, 3511 (2000)
27. Kowalczyk-Gajewska, K., Maj, M., Bieniek, K., Majewski, M., Opiela, K.C., Zieliński, T.G.: Cubic elasticity of porous materials produced by additive manufacturing: experimental analyses, numerical and mean-field modelling. Archives of Civil and Mechanical Engineering **24**(1) (2024). https://doi.org/10.1007/s43452-023-00843-z
28. Wu, Q., Xu, W., Zhang, L.: Microstructure-based modelling of fracture of particulate reinforced metal matrix composites. Compos. B Eng. **163**, 384–392 (2019). https://doi.org/10.1016/j.compositesb.2018.12.099
29. Nafar Dastgerdi, J., Anbarlooie, B., Miettinen, A., Hosseini-Toudeshky, H., Remes, H.: Effects of particle clustering on the plastic deformation and damage initiation of particulate reinforced composite utilizing x-ray ct data and finite element modeling. Compos. B Eng. **153**, 57–69 (2018). https://doi.org/10.1016/j.compositesb.2018.07.027
30. Węglewski, W., Bochenek, K., Basista, M., Schubert, T., Jehring, U., Litniewski, J., Mackiewicz, S.: Comparative assessment of Young's modulus measurements of metal-ceramic composites using mechanical and non-destructive tests and micro-CT based computational modeling. Comput. Mater. Sci **77**, 19–30 (2013)
31. Sequeira, A., Węglewski, W., Bochenek, K., Hutsch, T., Jarząbek, D., Weissgaerber, T., Basista, M.: Effect of SiC and Al2O3 reinforcements on the thermal conductivity of functionally graded AlSi12 matrix composites. Ceram. Int. **52**(5), 6399–6415 (2026). https://doi.org/10.1016/j.ceramint.2025.12.394
32. Sevostianov, I., Kushch, V.: Effect of pore distribution on the statistics of peak stress and overall properties of porous material. Int. J. Solids Struct. **46**(25), 4419–4429 (2009). https://doi.org/10.1016/j.ijsolstr.2009.09.002
33. Ma, H., Hu, G., Huang, Z.: A micromechanical method for particulate composites with finite particle concentration. Mech. Mater. **36**(4), 359–368 (2004). https://doi.org/10.1016/S0167-6636(03)00065-6
34. Kushch, V.I., Mogilevskaya, S.G., Stolarski, H.K., Crouch, S.L.: Elastic interaction of spherical nanoinhomogeneities with Gurtin-Murdoch type interfaces. J. Mech. Phys. Solids **59**(9), 1702–1716 (2011). https://doi.org/10.1016/j.jmps.2011.06.004
35. Rintoul, M.D., Torquato, S.: Metastability and crystallization in hard-sphere systems. Phys. Rev. Lett. **77**(20), 4198–4201 (1996). https://doi.org/10.1103/PhysRevLett.77.4198
36. Sequeira, A.: Thermal properties and thermal residual stresses in graded Al–matrix composites reinforced with Al_2O_3 and SiC particles: Experiments and numerical simulations. PhD thesis, Institute of Fundamental Technological Research, IPPT PAN, Warsaw, Poland (2025). https://www.ippt.pan.pl/repository/doktoraty/open/2025_sequeira_a_doktorat.pdf
37. Korelc, J.: Multi-language and multi-environment generation of nonlinear finite element codes. Eng. Comput. **18**(4), 312–327 (2002)
38. Schöberl, J.: Netgen an advancing front 2d/3d-mesh generator based on abstract rules. Comput. Vis. Sci. **1**(1), 41–52 (1997)
39. Šmilauer, V., Angelidakis, V., Catalano, E., Caulk, R., Chareyre, B., Chèvremont, W., Dorofeenko, S., Duriez, J., Dyck, N., Elias, J., Er, B., Gladky, A.E., Guo, N., Jakob, C., Kneib, F., Kozicki, J., Marzougui, D., Maurin, R., Yuan, C.: Yade Documentation, 3rd edn. The Yade Project, Computer Software (2021). 10.5281/zenodo.5705394 . http://yade-dem.org/doc/
40. Zieliński, T.G.: Generation of random microstructures and prediction of sound velocity and absorption for open foams with spherical pores. J. Acoust. Soc. Am. **137**(4), 1790–1801 (2015)
41. Kushch, V.I., Sevostianov, I.: Conductivity and elastic stiffness of spherical particle composite with partially disordered microstructure. International Journal of Engineering Science 162, 103473 (2021) 10.1016/j.ijengsci.2021.103473

42. Kowalczyk-Gajewska, K., Ostrowska-Maciejewska, J.: Review on spectral decomposition of Hooke's tensor for all symmetry groups of linear elastic material. Enging. Trans 57, 145–183 (2009). https://doi.org/10.24423/engtrans.172.2009